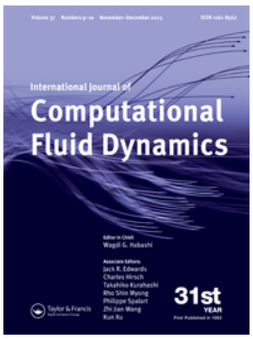

International Journal of Computational Fluid Dynamics

ISSN: (Print) (Online) Journal homepage: www.tandfonline.com/journals/gcfd20

Analysis of Slip Effects on the Stability and Interactions of Mach 5 Flat-Plate Boundary-Layer Waves

Lun Zhang, Zhongzheng Jiang, Hongwei Liu & Weifang Chen

To cite this article: Lun Zhang, Zhongzheng Jiang, Hongwei Liu & Weifang Chen (2023) Analysis of Slip Effects on the Stability and Interactions of Mach 5 Flat-Plate Boundary-Layer Waves, International Journal of Computational Fluid Dynamics, 37:9-10, 747-775, DOI: 10.1080/10618562.2024.2376096

To link to this article: https://doi.org/10.1080/10618562.2024.2376096

INTERNATIONAL JOURNAL OF COMPUTATIONAL FLUID DYNAMICS
2023, VOL. 37, NOS. 9–10, 747–775
https://doi.org/10.1080/10618562.2024.2376096

Taylor & Francis
Taylor & Francis Group

Analysis of Slip Effects on the Stability and Interactions of Mach 5 Flat-Plate Boundary-Layer Waves

Lun Zhang [a], Zhongzheng Jiang [a], Hongwei Liu [b] and Weifang Chen [a]

[a]School of Aeronautics and Astronautics, Zhejiang University, Hangzhou, People's Republic of China; [b]State Key Laboratory of High Temperature Gas Dynamics, Institute of Mechanics, Chinese Academy of Sciences, Beijing, People's Republic of China

ABSTRACT

The issue of boundary-layer transition with slight rarefaction for high-speed aircraft has recently received increased attention. In this paper, the stability and resonant interactions of boundary-layer waves for a Mach 5 flat plate under the slip effect are investigated using direct numerical simulation (DNS) and linear stability theory (LST). The slip effect is modelled by slip boundary conditions within the Navier-Stokes (NS) framework, and an LST method considering wall perturbations for both no-slip and slip flows is established. The present numerical results indicate that the slip effect has a consistent impact on the stability of fast and slow modes as obtained from DNS and current LST. In addition, the DNS results show that the slip effect delays the conversion of mode F_1 to mode S led by their resonance, and enhances the resonant interactions between fast mode waves and fast acoustic waves.

ARTICLE HISTORY
Received 24 July 2023
Accepted 29 June 2024

KEYWORDS
Boundary-layer stability; slip effects; direct numerical simulation; linear stability analysis; resonant interactions

1. Introduction

The study of boundary-layer transition is crucial for the development of high-speed vehicles (Lin 2008). When flying across the Earth's atmosphere, the aircrafts may encounter the laminar-turbulent transition, leading to a significant increase in drag force and aerodynamic heating (Hollis 2012). Moreover, these vehicles experience different flow regimes, ranging from continuum to rarefied flows (Ivanov and Gimelshein 1998). Recent research on transition has shifted their attention towards the flight altitude of 35–60 km (Klothakis et al. 2022; Ou and Chen 2021; Klothakis et al. 2021), where the flow instability and transition are still possible (Horvath et al. 2012; Thompson et al. 1998), while rarefaction effects can affect the local flow fields at certain locations on the aircraft surface (Boyd, Chen, and Candler 1995). As a new arising interest, the uncertainties of boundary-layer stability and transition combined with rarefaction effects, especially the slip-wall effects in the slip regime, may pose new challenges to the design of high-speed aircraft. Although studies on flow stability and transition coupled with rarefactions have received increased attention (Klothakis et al. 2022; 2021; Ou and Chen 2021; Tumuklu, Levin, and Theofilis 2018; Sawant, Theofilis, and Levin 2022; He, Zhang, and Cai 2019), many of the critical mechanisms involved still require further exploration.

In the past few decades, the high-speed boundary-layer transition has been extensively studied (Fedorov 2011; Reed, Saric, and Arnal 1996). In the flight environment with small disturbances, boundary-layer transition typically undergoes three stages: (1) The receptivity process whereby external free-stream disturbances excite boundary-layer waves. (2) Eigenmode growth. (3) Nonlinear breakdown to turbulence. The second stage of transition process has been widely studied by linear stability theory (LST) (Reed, Saric, and Arnal 1996). According to Mack (1975; 1984), there are multiple inviscid unstable modes in high-speed boundary layers besides the conventional viscous mode (i.e. the first mode which is the counterparts of Tollmien-Schlichting waves). Among these inviscid modes, the lowest-frequency one is called as the second mode whose instability generally dominates in high-speed boundary layers. Fedorov et al. (Fedorov and Khokhlov 2001; Fedorov and Tumin 2011) attempted to propose a new terminology of

CONTACT Zhongzheng Jiang jzhongzh@zju.edu.cn

boundary-layer waves for addressing the receptivity process. Specifically, the discrete modes in the eigenvalue spectra originating from fast acoustic waves are termed as 'fast modes', i.e. F_1, F_2, etc. based on the appearance sequence. The mode tuned to slow acoustic waves is termed as 'slow mode', which is designated S. Near the leading edge, mode S might be unstable, which represents Mack's first mode. Then, as mode F_1 and mode S synchronise, one mode becomes unstable and the other gets stabilised, and Mack's second mode refers to the unstable mode after synchronisation. Generally, mode S is unstable and constitutes Mack's first and second mode. Further downstream, mode S synchronises with mode F_2, F_3 and other fast modes to induce Mack's higher modes. There are numerous studies (Park et al. 2023; Han and Cao 2019; Liu et al. 2021; Park and Park 2023) so far devoting to understanding the high-speed boundary-layer stability based on LST.

Though these findings provide a clear understanding of high-speed boundary-layer transition, conducting thorough research on the topic remains challenging. Direct numerical simulation (DNS), which captures precise details of flow by solving full Navier-Stokes (NS) equations, has become a powerful tool for studying boundary-layer transitions with the developments of computers. Ma and Zhong (2003a; 2003b; 2005) performed a series of studies on the receptivity of a Mach 4.5 flat plate to free-stream disturbances by DNS and LST. They numerically studied the synchronisation process and revealed that the resonant interactions of boundary-layer waves are critical in the receptivity of unstable modes' excitation. Egorov et al. (2006) have performed a 2D DNS of the Mach 6 flat-plate boundary layer with wall blowing-suction to study the nonlinear saturation of fundamental harmonic and rapid growth of higher harmonics. Using LST and DNS, Knisely and Zhong (2019a; 2019b) conducted the work which confirmed the existence of supersonic mode and showed some of its overarching characteristics. To acquire a deeper understanding into the receptivity process, Kara et al. (2011; 2007) and Balakumar et al. (Balakumar and Kegerise 2011; Balakumar et al. 2018) performed a series of DNS of the receptivity of blunt cones. They found that the amplitudes of unstable waves induced by the slow acoustic waves are much larger than those resulting from the fast acoustic waves, except in the cases with cooling walls. Wan et al. (2018; 2020) developed a strategy to separately study different receptivity routes for the blunt cone. They revealed that due to the interaction between the slow acoustic wave and the bow shock, the fast acoustic wave is generated near the nose while the generated slow acoustic wave is transmitted downstream. In addition, Chen et al. (2021) investigated the receptivity of the second mode for the Mach 6 flow over a blunt wedge through DNS. The results show that the nonmodal disturbances in the entropy layer play a leading role in the excitation of the second mode. With broadband frequency disturbance spectra considered, He and Zhong (2021) used LST and DNS to study the receptivity of flow over a Mach 10 cone. It is found that the planar fast acoustic pulse is proven to much more readily excite modal waves other than the primary second mode. Recently, Ba et al. (2023) numerically investigated the hypersonic boundary-layer receptivity to planar and axisymmetric freestream slow acoustic waves for a Mach 6 flow over a circular cone with three different ellipsoidal/spherical noses. The receptivity mechanisms for both unstable modes were found to be similar to those for the sphere-nosed cone, and the variation of the receptivity coefficient with the frequency was also obtained. More DNS research on the receptivity, stability and transition of high-speed boundary layers can refer to the review paper of Zhong et al. (Zhong and Wang 2012).

Previous studies in the continuum regime have provided a foundation for the current research on high-speed boundary-layer transition with slight rarefactions. When the flows in different regimes are involved, however, it is necessary to adjust the computational approach accordingly. The choice of numerical method depends on the flow regime, which is typically classified by the Knudsen number Kn. This parameter represents the ratio of the molecular mean free path to a characteristic length (Moss and Bird 2003) and determines the level of rarefaction. The NS equations with no-slip boundary conditions are commonly used to simulate the flow in the continuum regime of $Kn < 0.001$. In the slip regime of $0.001 < Kn < 0.1$, where the effects of both the slip velocity and temperature jump occur near the wall, the Maxwell-Smoluchowski boundary models (Maxwell 1879; von Smoluchowski 1898) are widely adopted with the NS equations to solve for the flow. For highly rarefied gas flows ($Kn > 0.1$) in the transition and free molecular regimes, methods based on kinetic theory or high-order moment equations (Yang et al. 2022;

Jiang et al. 2021; Zhong, MacCormack, and Chapman 1993; Guo, Li, and Xu 2023; Myong and Xu 2021; Ragta, Srinivasan, and Sinha 2017) are required beyond NS framework. The kinetic theory can be used in all flow regimes and has been applied to study flow stability at the molecular levels (Klothakis et al. 2022; Tumuklu, Levin, and Theofilis 2018; Sawant, Theofilis, and Levin 2022; Manela and Zhang 2012). However, due to their high computational cost, the methods based on NS equations with slip boundary are preferred for the slip-regime flows. Figure 1(a) illustrates the schematic of the present physical problem. Based on the definition of Knudsen number, the rarefaction effects can also be classified into two categories. One is related to the free-stream rarefaction effect that takes effect in front of shock preceding the leading edge, representing the insufficient interactions between the gas molecules. The other is about the slip effect occurring at wall inside the viscous sublayer of boundary layer. The latter is induced by the insufficient collision of gas and solid molecules subject to the local small characteristic length of leading-edge configuration, as shown in Figure 1(b). It is inferred that the free-stream rarefaction has a strong connection with the receptivity mechanisms, whereas the slip effect at the wall mainly affects the development process of boundary-layer waves. In this study, the impact of slip wall on the boundary-layer waves is the primary object.

In fact, numerous studies have investigated the impacts of slip velocity on the boundary-layer stability (Liu and Zhang 2020; Chai and Song 2019), particularly over hydrophobic/super-hydrophobic surfaces (Choi, Westin, and Breuer 2003; Abu Rowin, Hou, and Ghaemi 2017; Samaha and Gad-el Hak 2021) in incompressible flows. However, in recent years, there has been growing interest in studying the boundary-layer stability of compressible slip flows. He et al. (2019) initially investigated the impact of slip velocity on the supersonic flat-plate boundary-layer stability by LST, and reported that the second mode is stabilised by the slip velocity. Subsequently, Klothakis et al. (2022) utilised LST to obtain the eigenvalue spectrum for rarefied compressible flat-plate boundary layers at an altitude of 55 km based on the steady solutions computed by direct simulation Monte Carlo (DSMC). They found that the slip velocity and temperature jump could stabilise the discrete eigenmode. However, previous analyses of LST did not consider wall perturbations of temperature and velocity induced by the slip boundary. By considering different wall perturbation boundary conditions in LST, Ou and Chen (2021) systematically studied linear stability of Mack modes for a slightly rarefied supersonic boundary layer under the NS framework. The influence of slip perturbation boundary on the stability is discussed and their results shed a light on the compressible slip boundary-layer stability from a macroscopic point of view. These pioneering LST studies provide us inspirations and preliminary insights into the boundary-layer stability of compressible slip flows.

Given that the LST method has certain limitations, e.g. it is based on the parallel-flow assumption and cannot resolve modal interactions, there remain many unanswered questions regarding the slip effect on boundary-layer stability. For instance, it is unclear whether the previous findings are still valid under a more realistic numerical or experimental environment, as they have not been supported by numerical simulations or experiments yet. Additionally, the impact of slip effect on the interactions between wave modes is unknown but these interactions are crucial factors in the study of receptivity (Ma and Zhong 2003a; 2003b; 2005). Answering these questions would provide important insights into the fundamental mechanisms of slip flows and contribute to the development for predicting and controlling boundary-layer transitions.

Accordingly, we aim to investigate the linear stability and resonant interactions of boundary-layer waves for a Mach 5 flat plate in the slip regime by both DNS and LST in this paper. Unlike previous pure LST studies, DNS offers the advantage of making fewer limiting assumptions and can resolve interactions between modes. The effects of slip velocity and temperature jump are both considered and modelled by slip boundary conditions within the NS framework. The NS equations with both no-slip and slip boundary conditions are accurately solved to obtain steady flows. Subsequently, unsteady direct numerical simulations are carried out to show the spatial developments of mode F and mode S under various degrees of the slip effect. As it is difficult to produce mode S or mode F in experiments, numerical simulations offer the advantage of using pure mode to simplify the problem. These unsteady simulations reveal the impact of slip wall

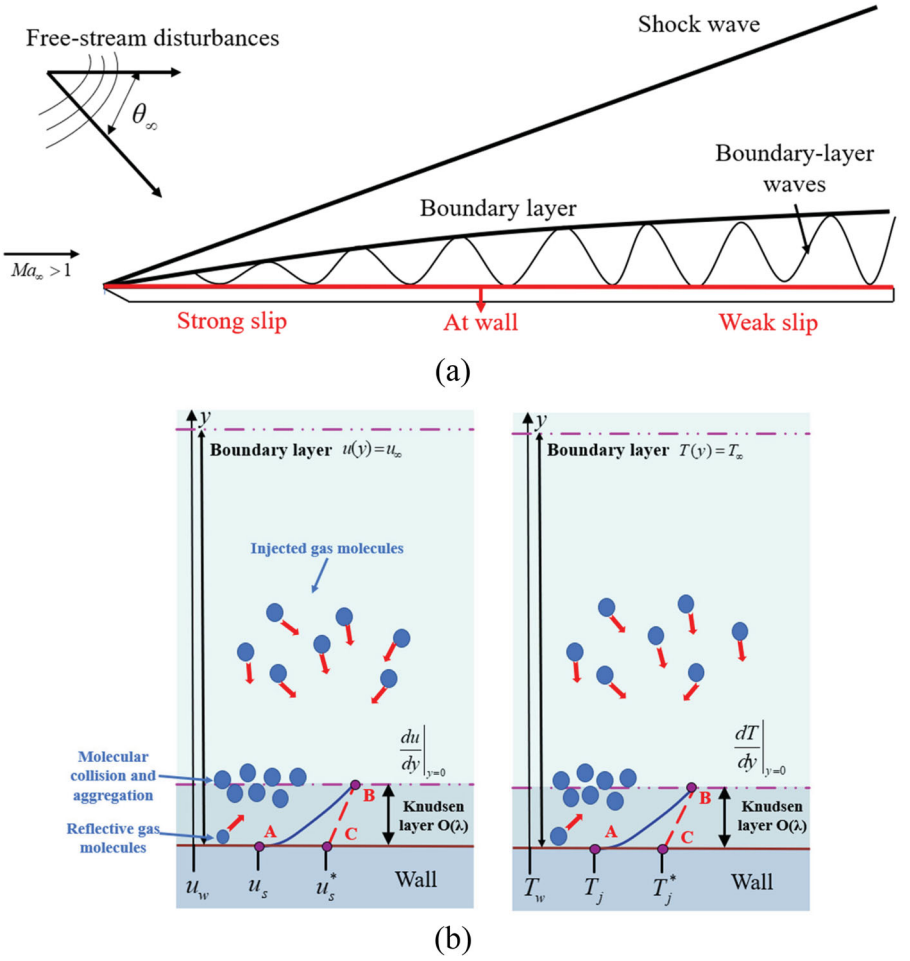

Figure 1. (a) The diagram of the process from receptivity to boundary-layer instability for a supersonic flat-plate flow at relatively high altitudes (35 ∼ 60 km). (b) The schematic of slip effects at the wall.

on both the linear stability and the resonant interactions of boundary-layer waves. Moreover, the LST analysis that considers the perturbations of both no-slip and slip wall is conducted and compared with the numerical solutions.

This paper is arranged as follows. Section 2 presents the description of DNS, wall boundary models, LST with no-slip and slip wall perturbation boundary conditions and the computational setup. In Section 3, the slip effect on the linear stability and resonant interactions of boundary-layer waves is analysed using DNS and LST. Finally, conclusions are given in Section 4.

2. Problem Formulation and Methodology

2.1. Governing Equations and Numerical Methods

The governing equations are the three-dimensional (3D) nondimensional compressible Navier-Stokes (NS) equations expressed as

$$\frac{\partial}{\partial t}\boldsymbol{U}+\frac{\partial}{\partial x}\boldsymbol{F}_1+\frac{\partial}{\partial y}\boldsymbol{F}_2+\frac{\partial}{\partial z}\boldsymbol{F}_3=\frac{\partial}{\partial x}\boldsymbol{V}_1+\frac{\partial}{\partial y}\boldsymbol{V}_2+\frac{\partial}{\partial z}\boldsymbol{V}_3 \tag{1}$$

where $\boldsymbol{U}=[\rho,\rho u,\rho v,\rho w,E]^{\mathrm{T}}$ is a vector of conservative variables. $\boldsymbol{F}_1$, $\boldsymbol{F}_2$ and $\boldsymbol{F}_3$ are inviscid flux vectors, which can be written as

$$\boldsymbol{F}_1=\begin{bmatrix}\rho u\\ \rho u^2+p\\ \rho uv\\ \rho uw\\ u(E+p)\end{bmatrix},\ \boldsymbol{F}_2=\begin{bmatrix}\rho v\\ \rho uv\\ \rho v^2+p\\ \rho vw\\ v(E+p)\end{bmatrix},$$

$$\boldsymbol{F}_3=\begin{bmatrix}\rho w\\ \rho uw\\ \rho vw\\ \rho w^2+p\\ w(E+p)\end{bmatrix}. \tag{2}$$

The viscous and diffusive flux vectors $\boldsymbol{V}_1$, $\boldsymbol{V}_2$ and $\boldsymbol{V}_3$ are expressed as.

$$\boldsymbol{V}_1 = \frac{1}{Re_\infty}\begin{bmatrix} 0 \\ \tau_{11} \\ \tau_{21} \\ \tau_{31} \\ u\tau_{11} + v\tau_{21} + w\tau_{31} + k\dfrac{\partial T}{\partial x} \end{bmatrix},$$

$$\boldsymbol{V}_2 = \frac{1}{Re_\infty}\begin{bmatrix} 0 \\ \tau_{12} \\ \tau_{22} \\ \tau_{32} \\ u\tau_{12} + v\tau_{22} + w\tau_{32} + k\dfrac{\partial T}{\partial y} \end{bmatrix},$$

$$\boldsymbol{V}_3 = \frac{1}{Re_\infty}\begin{bmatrix} 0 \\ \tau_{13} \\ \tau_{23} \\ \tau_{33} \\ u\tau_{13} + v\tau_{23} + w\tau_{33} + k\dfrac{\partial T}{\partial z} \end{bmatrix}, \quad (3)$$

where ρ denotes the density; u, v and w are the velocity components in the Cartesian coordinates; T is the temperature; E is the total energy; Re_∞ denotes the freestream Reynolds number; and p, τ are the pressure and the stress tensor, respectively, calculated as follows:

$$p = \frac{\rho T}{\gamma\, Ma_\infty^2},$$

$$\tau_{ij} = \begin{cases} \mu\left(\dfrac{\partial u_i}{\partial x_j} + \dfrac{\partial u_j}{\partial x_i}\right), & i \neq j. \\ 2\mu\dfrac{\partial u_i}{\partial x_i} - \dfrac{2}{3}\mu\nabla\cdot\boldsymbol{u}, & i = j. \end{cases} \quad (i,j = 1,2,3) \quad (4)$$

The heat conductivity coefficient $k = C_p\mu/Pr$ is computed with $Pr = 0.72$. Ma_∞ is the freestream Mach number and γ is the specific heat ratio. The dynamic viscosity μ is calculated by the Sutherland's law. The flow variables are normalised by the corresponding freestream parameters with the subscript ∞. The length variable is scaled by the reference length L^*, with time by L^*/u_∞^*. Hereinafter, the superscript $*$ denotes the dimensional variables, and the dimensionless variables are denoted with no superscript. In this paper, our work primarily focuses on investigating two-dimensional (2D) planar waves, while also conducting simulated analyses of specific 3D oblique waves. To optimise computational resources, we primarily utilise the 2D NS equations. However, when studying the streamwise development of oblique waves, we employ the 3D NS equations. The 2D governing equations can be derived by disregarding the spanwise-direction variables in the 3D governing equations.

The fifth-order weighted essentially non-oscillatory scheme is used for the discretisation of inviscid flux derivatives, and the sixth-order central scheme is used for viscous flux derivatives. Moreover, a third-order Runge–Kutta method is applied for time marching. The current DNS code has been widely used to simulate high-speed boundary-layer transition and turbulence (Li, Fu, and Ma 2010; Liang and Li 2013; Qi et al. 2021).

2.2. Wall Boundary Model

Under the NS framework, conventional no-slip isothermal wall boundary conditions are used to simulate the no-slip flow. To simulate the slip flow, the Maxwell-Smoluchowski (M-S) slip boundary model (Maxwell 1879; von Smoluchowski 1898) is adopted to depict the slip velocity and temperature jump at the wall and can be expressed as

$$V_{\text{slip}}^* = \frac{2-\sigma_u}{\sigma_u}\lambda^*\left.\frac{\partial V^*}{\partial n}\right|_{\text{wall}},$$

$$T_{\text{slip}}^* = T_{\text{wall}}^* + \frac{2-\sigma_T}{\sigma_T}\frac{2\gamma}{\gamma+1}\frac{\lambda^*}{Pr}\left.\frac{\partial T^*}{\partial n}\right|_{\text{wall}}, \quad (5)$$

and

$$\lambda^* = \frac{\mu^*}{\rho^*}\sqrt{\frac{\pi}{2R^*T^*}}, \quad (6)$$

where V_{slip}^* and T_{slip}^* are the slip velocity and jump temperature, respectively; V^* represents the velocity component tangent to the wall; n represents the wall-normal direction; λ^* is the mean free path of gas molecules; R^* is the gas constant; T_{wall}^* denotes the wall temperature; σ_u and σ_T are the tangential momentum accommodation coefficient and the thermal accommodation coefficient, respectively. The specific values of the surface accommodation coefficients depend on gas composition and surface properties such as surface roughness and contamination (Zhang, Meng, and Wei 2012). Many studies have been carried out to obtain σ_u and σ_T for the certain gas-surface interaction (Trott et al. 2011; Graur et al. 2009). The results indicate that

they may differ from each other. In general, the accommodation coefficients are close to 1, but lower values are also possible when the surface is smoother or the incoming velocity is higher. In this study, σ_u and σ_T are assumed equal and are uniformly symbolised by σ. Moreover, σ varies as 1.0 and 0.4 to model different degrees of slip wall, respectively.

2.3. Linear Stability Theory for no-slip and Slip Flows

The LST is used to analyse the stability of boundary-layer waves. The disturbance in LST is assumed to be a wave ansatz. The instantaneous variable $\phi = [\rho, u, v, w, T]$ and disturbance $\phi' = [\rho', u', v', w', T']$ with the parallel-flow assumption are described as

$$\phi = \overline{\phi} + \phi', \tag{7}$$

and

$$\phi' = \widehat{\phi}(y)\exp[i(\alpha x + \beta z - \omega t)], \tag{8}$$

where the overbars '–' and '∧' represent the mean quantity and the complex eigenfunction, respectively; α and β are the streamwise wavenumber and spanwise wavenumber, respectively, and ω is the circular frequency. The wavenumber and circular frequency are normalised by $1/L^*$ and u^*_∞/L^*, respectively. Substituting Equation (8) and steady base flow into the linearised compressible NS equations, an ordinary differential equation (ODE) system is obtained as

$$\left(A\frac{d^2}{dy^2} + B\frac{d}{dy} + C\right)\widehat{\phi} = 0\,, \tag{9}$$

where the flow variables are scaled by the corresponding quantities at the boundary-layer edge. The coefficients A, B and C are 5×5 complex matrixes and more details could be referred to Malik's paper (Malik 1990). The reference length is given by $L^* = \sqrt{\mu^*_\infty x^*/\rho^*_\infty u^*_\infty}$, and the Reynolds number based on L^* is generally used and defined as

$$Re_L = \frac{\rho^*_\infty u^*_\infty L^*}{\mu^*_\infty}\,. \tag{10}$$

For the no-slip flow, the perturbation boundary conditions of Equation (9) are commonly given as

$$y = 0\text{: } \widehat{u} = \widehat{v} = \widehat{w} = \widehat{T} = 0\,, \tag{11}$$

$$y \to \infty\text{: } \widehat{u}, \widehat{v}, \widehat{w}, \widehat{T} \to 0\,. \tag{12}$$

Here, Equation (11) denotes the perturbation boundary condition of the no-slip wall, which assumes the disturbance of both velocity and temperature to be zero at the wall.

However, in the slip-regime flow, there exist perturbations of both velocity and temperature at the wall due to the existence of velocity slip and temperature jump. These perturbations should therefore be modelled because they are not trivial. Since the instantaneous flow can still be deemed as fulfilling the M-S slip model, perturbation boundary conditions at the wall can be derived by linearising Equation (5). This leads to the 'slip-wall perturbation boundary conditions' stated as

$$\begin{aligned} y = 0 :\ \widehat{u} &= \frac{2-\sigma_u}{\sigma_u}\left(\overline{\lambda}\frac{\partial\widehat{u}}{\partial y} + \frac{\partial\overline{u}}{\partial y}\widehat{\lambda}\right), \\ \widehat{w} &= \frac{2-\sigma_u}{\sigma_u}\left(\overline{\lambda}\frac{\partial\widehat{w}}{\partial y} + \frac{\partial\overline{w}}{\partial y}\widehat{\lambda}\right), \\ \widehat{T} &= \frac{2-\sigma_T}{\sigma_T}\frac{2\gamma}{(\gamma+1)Pr}\left(\overline{\lambda}\frac{\partial\widehat{T}}{\partial y} + \frac{\partial\overline{T}}{\partial y}\widehat{\lambda}\right). \end{aligned} \tag{13}$$

Here, the fluctuation of molecular mean free path $\widehat{\lambda}$ can be obtained by differentiating Equation (6) and is given as

$$\begin{aligned} \widehat{\lambda} &= \frac{\partial\lambda}{\partial\rho}\widehat{\rho} + \frac{\partial\lambda}{\partial \mathrm{T}}\widehat{\mathrm{T}} + \frac{\partial\lambda}{\partial\mu}\widehat{\mu} \\ &= \frac{Ma}{Re_L}\sqrt{\frac{\pi\gamma}{2}}\left(\frac{1}{\overline{\rho}\sqrt{\overline{T}}}\widehat{\mu} - \frac{\overline{\mu}}{\overline{\rho}^2\sqrt{\overline{T}}}\widehat{\rho} - \frac{\overline{\mu}}{2\overline{\rho}}\frac{1}{\overline{T}^{\frac{3}{2}}}\widehat{\mathrm{T}}\right). \end{aligned} \tag{14}$$

Here $\widehat{\mu} = (d\mu/dT)\widehat{\mathrm{T}}$. Equation (13) shows that for slip flow, each perturbation for velocity and temperature at the wall consists of two terms. The first term represents the contribution of the perturbation gradient and the mean free path of gas molecules near the wall. The second term denotes the product of the gradient of base flow and the fluctuation of mean free path, which is non-negligible in high-speed compressible flows, particularly with rarefaction. As shown in Equation (14), the fluctuation of mean free path gets significant as compressibility effects or rarefaction degrees are strengthened, i.e. Ma increases or Re decreases. It is evident that Equation (13) automatically transforms to the conventional no-slip perturbation boundary condition when $Kn \propto Ma/Re$ is small enough.

Table 1. Flow conditions of the free stream.

Ma_∞	p^*_∞(Pa)	T^*_∞(K)	Re^*_∞(m^{-1})	ρ^*_∞(kg · m^{-3})	γ
5.0	135.3	65.15	1.34×10^6	7.23×10^{-3}	1.4

Accordingly, Equations (9), (11) and (12) constitute an eigenvalue problem for no-slip flows, whereas Equations (9), (12) and (13) constitute the eigenvalue problem for slip flows. In the spatial LST, ω and β are real while $\alpha = \alpha_r + i\alpha_i$ is a complex eigenvalue. If $\alpha_i < 0$, the flow is unstable with the spatial growth rate $-\alpha_i$. The present purpose is to solve the complex dispersion relation expressed as $\alpha = \alpha(Re_L, \omega, \beta)$. For the discretisation of the ODE system, both the single domain Chebyshev spectral collocation method and the fourth-order compact difference method are utilised in our in-house code. The validation of our LST code is given in the Appendix.

2.4. Computational Setup

A flat-plate boundary layer with $Ma_\infty = 5$ is considered, and the fluid is the perfect gas with constant specific heat. The details of free-stream conditions are given in Table 1, and the free-stream density and pressure are corresponding to flight at an altitude around 40 km. The Reynolds number in the table is the unit Reynolds number with $Re^*_\infty = \rho^*_\infty u^*_\infty / \mu^*_\infty$. The wall temperature T^*_w is set as 300 K, which is about 0.88 times the recovery temperature T^*_r defined as $T^*_r = T^*_\infty \left[1 + (\gamma - 1)\sqrt{\mathrm{Pr}} Ma^2_\infty / 2\right]$.

For each no-slip and slip flow scenario, the investigation process consists of two steps. First, the steady solution is calculated to provide the base flow, and the LST analysis with corresponding wall perturbation boundary conditions is carried out. Second, unsteady simulations are performed by introducing waves of mode F_1, F_2 and S, respectively, to study their spatial evolutions.

The rectangular computational domain of steady simulations is set as $0 \le x^* \le 2.0$ m and $0 \le y^* \le 0.1$ m. Totally 8001 grid nodes are distributed in the streamwise direction, and there are adequate nodes near the leading edge to depict the shock wave. In the wall-normal direction, an exponential grid stretching function is used with 201 grid nodes to cluster more points inside the boundary layer. In the unsteady simulations, a 2D computational domain is utilised for all cases, except when simulating the evolution of oblique mode S waves with a fixed spanwise wavenumber, for which a 3D computational domain is employed. The 2D unsteady computational domain is prolonged to $x^* = 2.3$ m and the gird scale is the same as that of the steady simulations. To suppress disturbances reflected from the outlet boundary, the buffer region extends from $x^* = 1.95$ m to $x^* = 2.3$ m with aggressive grid stretching. The 3D unsteady computational domain is set as $0.1 \le x^* \le 1.5$ m, $0 \le y^* \le 0.1$ m and $0 \le z^* \le 0.07392$ m, and the buffer region extends from $x^* = 1.2$ m to $x^* = 1.5$ m. The spanwise computational length corresponds to a spanwise wavelength of the oblique wave with the given disturbance parameters. In 3D computations, the grid resolution in the streamwise and wall-normal directions is consistent with that of the 2D unsteady simulation. In the spanwise direction, there are 120 grid nodes equally spaced. The study of computational reliability and grid independence is provided in the Appendix.

In both steady and unsteady simulations, no-slip isothermal and M-S slip boundary conditions are imposed at the wall, respectively, to simulate flows under different degrees of the slip effect. For the two lateral boundaries in 3D unsteady simulations, periodic boundary conditions are employed. In addition, special treatment of the inlet and outlet boundary is used. In steady simulations, the inlet boundary is designated as free-stream conditions and the supersonic outlet is adopted. In unsteady simulations, the non-reflection boundary conditions are used at the outlet. At the inlet of unsteady simulations, disturbances corresponding to mode S or mode F are superimposed on the steady base flow, i.e.

$$\begin{aligned}\phi(x_{\mathrm{inlet}}, y, z, t) &= \overline{\phi}(x_{\mathrm{inlet}}, y, z) + \varepsilon \widehat{\phi}(x_{\mathrm{inlet}}, y) \\ &\quad \times \exp[i(\alpha_r x_{\mathrm{inlet}} - \omega t - \beta z)] + \text{c.c.}\,, \end{aligned} \tag{15}$$

where x_{inlet} is the streamwise location of inlet, and c.c. is the complex conjugate. The disturbance amplitude ε is assigned as 1×10^{-5} in this study to ensure the linear evolution of disturbances. For mode waves at a fixed frequency and spanwise wavenumber, the wavenumber α_r and the eigenfunction $\widehat{\phi}(x_{\mathrm{inlet}}, y)$ are obtained from LST. This way of introducing directly fast mode waves or slow mode waves has been adopted by some previous DNS studies (Ma and Zhong 2003a; Wang and Zhong 2012) to study the mechanism of

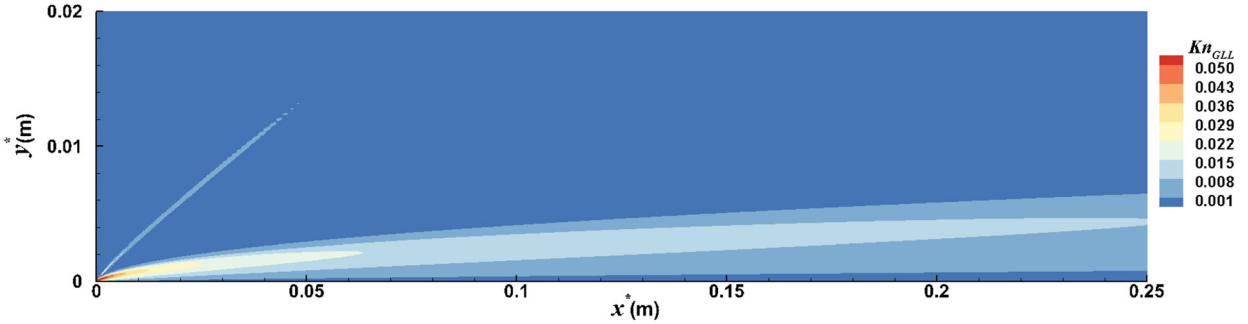

Figure 2. The contour of gradient-length local Knudsen number over the plate for the slip flow $\sigma = 1.0$.

boundary-layer waves. Moreover, it has been studied that the development of boundary-layer waves induced by this way is similar to that in the case where the disturbances are generated through the leading-edge receptivity to free-stream acoustic waves (Ma and Zhong 2003b). The frequency in unsteady simulations is characterised by a dimensionless frequency F defined as

$$F = \frac{\omega^* \mu_\infty^*}{\rho_\infty^* {u_\infty^*}^2}. \tag{16}$$

The relationship between ω and F is

$$\omega = F \times Re_L. \tag{17}$$

3. Results and Discussions

3.1. Steady Flow Analysis

(1) Base flows

This section presents the steady solutions of the Mach 5 flow for no-slip and slip cases. Figure 2 shows the contour of the gradient-length local Knudsen number Kn_{GLL} near the leading edge for the slip flow with $\sigma = 1.0$. The Kn_{GLL} was proposed by Boyd et al. (1995) to quantify the degree of rarefaction in the local region of flow field, which is defined as

$$Kn_{GLL} = \frac{\lambda}{Q}\left|\frac{dQ}{dl}\right|, \tag{18}$$

where Q denotes a flow property, e.g. the density, and l represents the distance between two certain flowfield points, which should be taken along the direction of the steepest gradient of flow properties. In this study, the local Knudsen number near the leading edge is used to assess the degree of rarefaction in the flow, which affects the slip velocity and temperature jump at the wall. As depicted in in Figure 2, the global flow is continuous, but the local Knudsen number varies significantly along the flow direction, especially near the leading edge and the wall, where Kn_{GLL} is basically in the range of [0.001, 0.05], indicating the presence of slip effects. Given that the local flow is predominantly in the slip regime, it is reasonable to investigate the boundary-layer stability with the inclusion of slip effects under the NS framework. This approach enables us to model the flow behaviour over a range of Knudsen numbers and provides a foundation for understanding the impact of slip velocity and temperature jump on the boundary-layer stability.

Figure 3 shows the slip velocity and temperature jump along the plate surface of slip base flows. In slip flows, the distributions of slip velocity and jump temperature exhibit similar traits. Specifically, the slip velocity reaches maximum at the leading edge and decreases monotonously downstream, since the slip degree gradually weakens as x^* increases. The temperature, however, sharply rises at the leading edge, and then gradually declines downstream. This figure clearly illustrates that the slip effect would enhance as σ decreases. The wall-normal profiles of streamwise velocity and temperature at $x^* = 0.18$ m for no-slip and slip base flows are compared in Figure 4(a). As σ decreases, both the temperature jump and the slip velocity at the wall increase, while the boundary layer thickness δ decreases. This reduction of δ might be due to the increasing wall velocity, which is consistent with the principle of boundary-layer mass flow conservation. It can be inferred that the slip effect might increase the second-mode most unstable frequency, as the wavelength of the most unstable second-mode disturbance is roughly twice the boundary-layer thickness (Dash and Papp 2002). Figure 4(b) illustrates the impact of slip wall on the profiles of generalised inflection points (GIPs), which are crucial to the inviscid

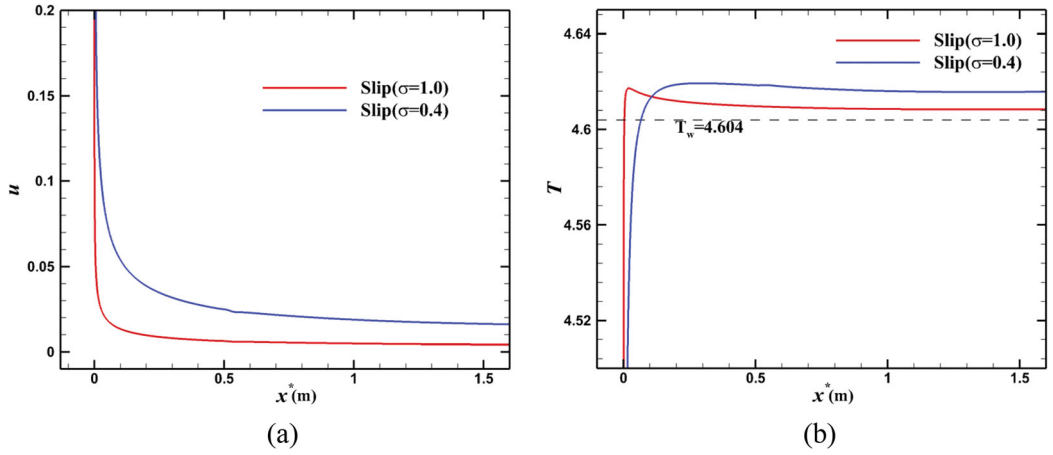

Figure 3. The distribution of (a) slip velocity and (b) temperature jump on the plate surface for slip base flows.

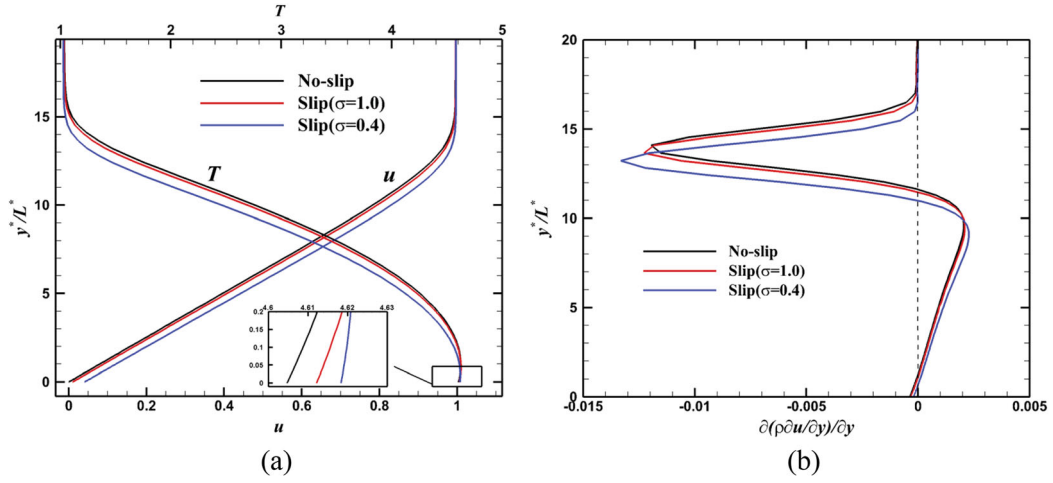

Figure 4. The profiles of (a) streamwise velocity and temperature and (b) GIPs defined as $\partial(\rho\partial u/\partial y)/\partial y$ for no-slip and slip base flows at $x^* = 0.18$ m.

instability in compressible flows. It can be seen that two GIPs exist in the boundary layer for both no-slip and slip cases, but the location of both GIPs moves closer towards the wall as the slip effect becomes more pronounced. The above differences in the mean flow indicate that the slip wall may have an effect on the boundary-layer stability.

(2) Linear stability analysis

This section presents the stability characteristics of modes F_1, F_2 and S for no-slip and slip cases analysed by LST. Figure 5(a) shows the distributions of phase velocity ($c_r = \omega/\alpha_r$) of modes F_1, F_2 and S in no-slip and slip cases at a frequency $F = 3.2 \times 10^{-4}$. The three horizontal dashed lines correspond to the phase velocities of fast acoustic waves, entropy/vorticity waves, and slow acoustic waves, respectively. The figure shows that the trajectories of phase velocity of boundary-layer waves in no-slip and slip flows are similar. Specifically, modes F_1 and F_2 originate from fast acoustic waves, while mode S originates from slow acoustic waves. As x^* increases, the phase velocities of fast modes decrease. The fast modes will synchronise with mode S when their curves intersect. At the synchronisation point, phase velocities of fast and slow modes are identical, and their eigenfunctions have a very similar profile as shown in Figure 6.

From Figure 5(a), the effect of slip boundary on the phase velocity of fast and slow modes can be observed. The phase velocities of fast modes drop more slowly in slip flows than in no-slip flows. In contrast, the phase velocity of mode S is almost unaffected by the slip boundary. Consequently, the synchronisation points between fast and slow modes are shifted downstream as the slip effect increases. Given that

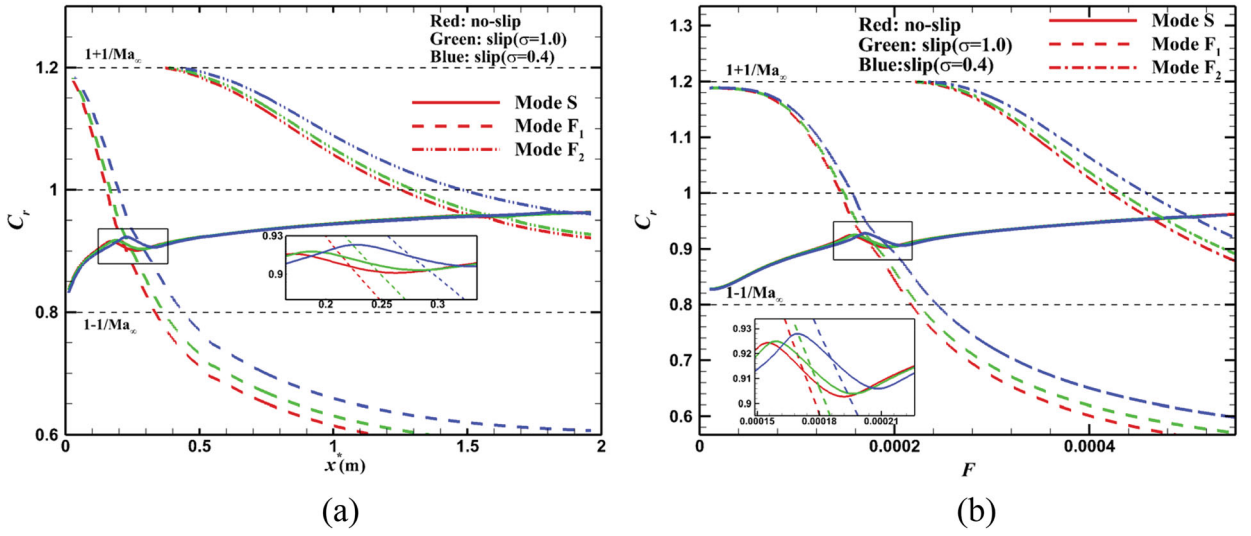

Figure 5. The slip effect on the phase velocity of modes F_1, F_2 and S ($\beta^* = 0$) at (a) a fixed frequency $F = 3.2 \times 10^{-4}$ and (b) a fixed streamwise location of $x^* = 0.746$ m.

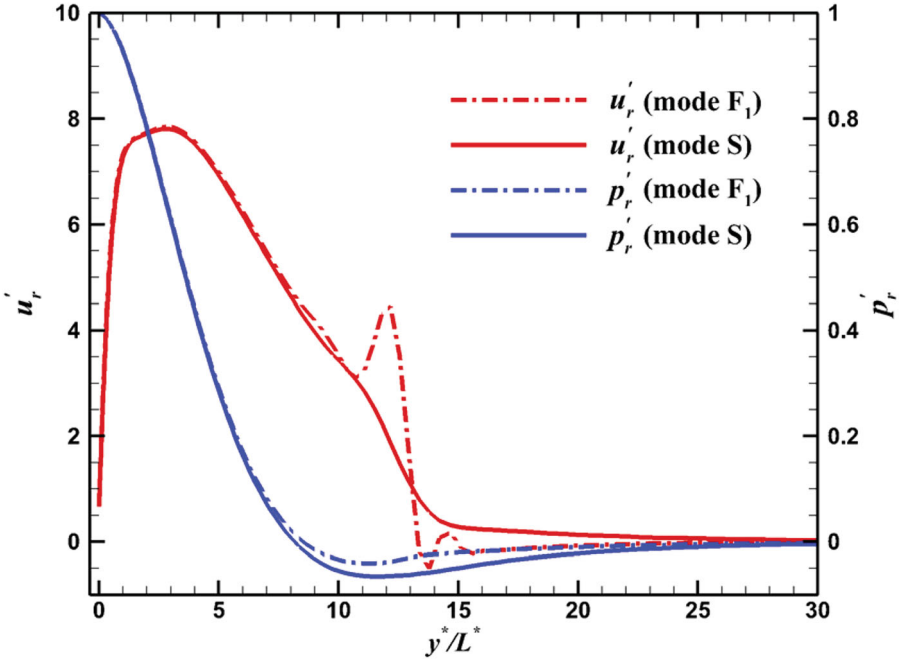

Figure 6. Eigenfunctions of streamwise velocity and pressure of mode F_1 and mode S ($\beta^* = 0$) at the synchronisation point in the slip flow ($\sigma = 1.0$).

the synchronisations of fast and slow modes induce Mack's second and higher modes, it is evident that the onset of these modes would be postponed in slip flows. Additionally, Figure 5 indicates that the slip effect also delays the synchronisation of fast modes and the entropy/vorticity waves but has little effect on the synchronisation of fast modes and fast acoustic waves. When the frequency or streamwise location is changed, above trends are still valid. For instance, Figure 5(b) shows the distribution of phase velocity at a fixed streamwise location, and the same tendency can be found. The synchronisation between above different waves can lead to their resonant interactions (Ma and Zhong 2003a), which will be further discussed in the next section.

The eigenfunctions of modes F_1, F_2 and S for no-slip and slip cases are compared in Figure 7, where the magnitude of disturbances of streamwise velocity and pressure at $x^* = 0.746$ m is shown. In this paper, the profiles of eigenfunctions are normalised by

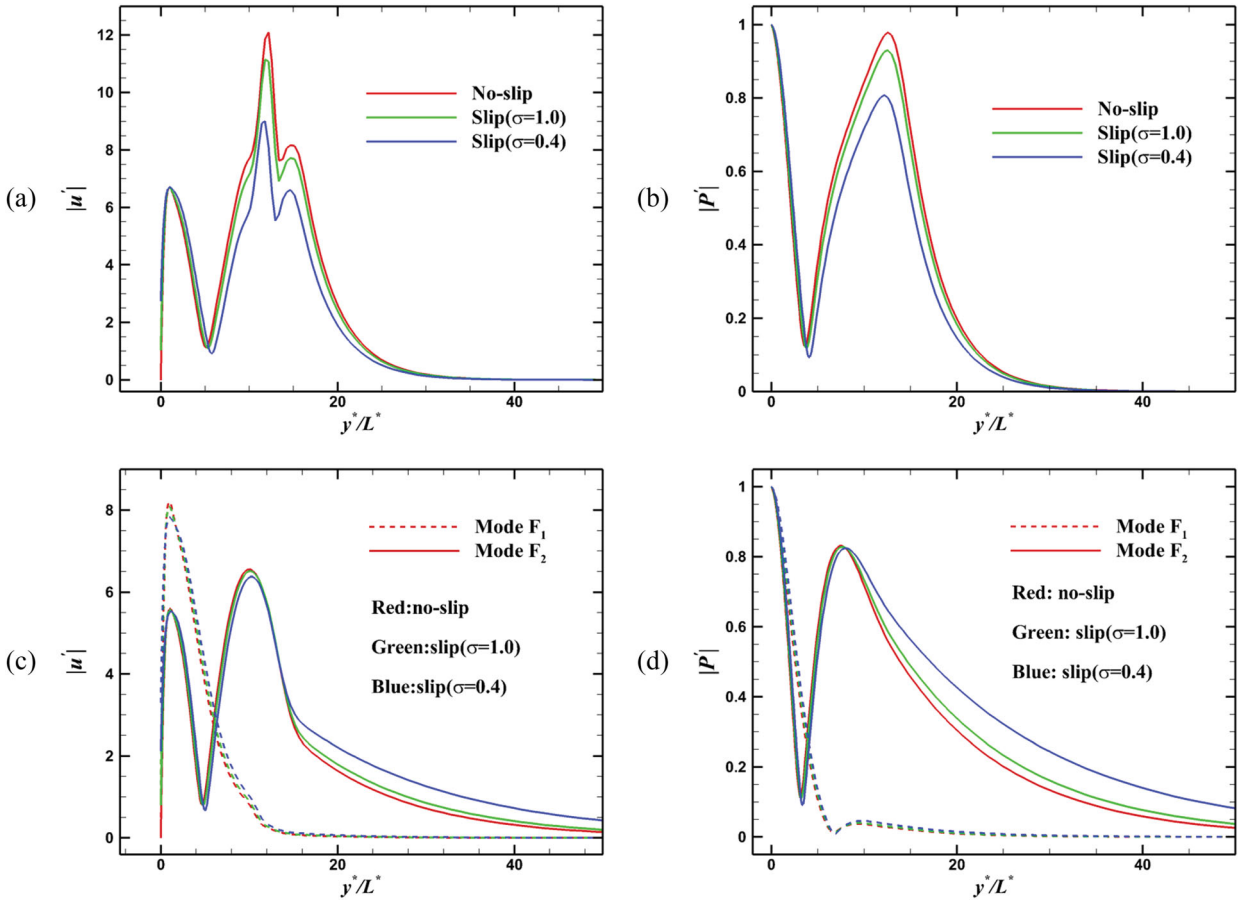

Figure 7. Comparisons of the eigenfunction magnitudes of streamwise velocity and pressure at $x^* = 0.746$ m between the no-slip and slip flows obtained by LST ($\omega = 0.26$, $\beta^* = 0$): (a) tangential velocity and (b) pressure of mode S; (c) tangential velocity and (d) pressure of modes F_1 and F_2.

the pressure perturbation at the wall. Figure 7 indicates that the slip boundary has little impacts on the eigenfunctions of fast and slow modes near the wall. However, the slip effect can generate the wall perturbation in both velocity and temperature, and this would affect the boundary-layer stability. These wall perturbations would amplify as the slip effect becomes more pronounced. Moreover, disturbances both inside and outside the boundary layer are indeed affected by the slip boundary. In general, as the slip effect enhances, the magnitudes of disturbances for mode S decline while the ones for both mode F_1 and F_2 increase. These observations highlight the complex and multifaceted nature of slip flows, as well as the importance of accurately modelling and characterising their behaviour.

Figure 8(a) compares the growth rate $-\alpha_i$ of 2D modes F_1, F_2 and S at the streamwise location of $x^* = 0.746$ m for no-slip and slip flows. It shows that the fast modes are always stable in slip flows, but their decay rates are lower than those of the no-slip flow. Depending on the area upstream or downstream of its synchronisation point with mode F_1, mode S is either termed as the first mode or second mode as marked in the figure. The figure shows that the the first-mode growth rate is increased whereas the second-mode growth rate is slightly decreased due to the impact of slip wall. The maximum growth rate of 2D mode S at different streamwise locations for no-slip and slip cases is given in Figure 8(b). It is evident that the slip velocity and temperature jump stabilise the second mode but destabilise the first mode, which is consistent with the finding of Ou and Chen (2021). Furthermore, Figure 8(a) shows that the second-mode most unstable frequency increases as σ decreases, which is related to the decrease of boundary-layer thickness.

Given that the oblique first-mode instability is also important in high-speed boundary layers (Mack 1984), the stability of oblique mode S waves is investigated. Figure 9 presents the distribution of growth rate for 3D mode S waves at different wave angles

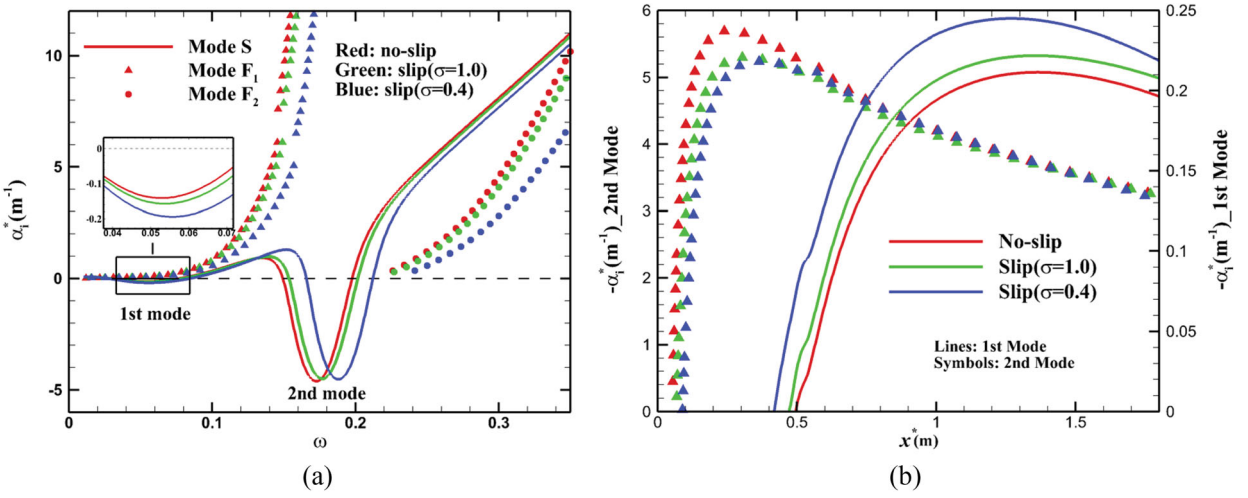

Figure 8. The slip effect on the (a) growth rates of boundary-layer waves at $x^* = 0.746$ m and (b) maximum growth rates of two-dimensional mode S ($\beta^* = 0$) at different streamwise locations.

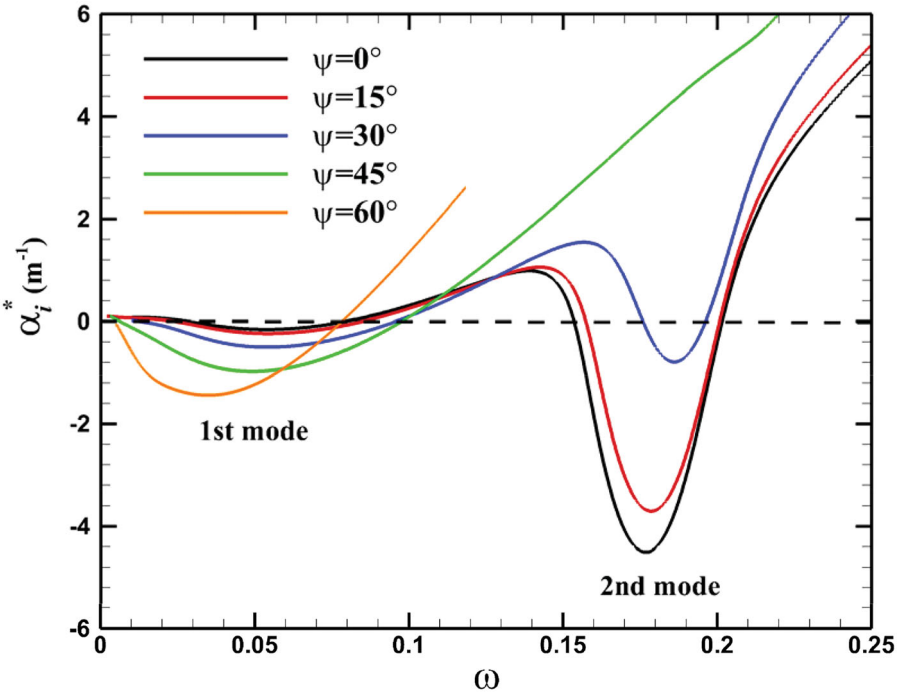

Figure 9. The variation of growth rate with angular frequency at $x^* = 0.746$ m of three-dimensional mode S waves at different wave angles in the $\sigma = 1.0$ slip flow.

$\psi = \arctan(\beta/\alpha_r)$ in the $\sigma = 1.0$ slip flow. The results clearly indicate that the oblique wave with a specific wave angle is the most unstable for the first mode, whereas the 2D wave ($\psi = 0°$) is the most unstable for the second mode. Moreover, the 2D second-mode instability dominates under the current conditions of Mach 5 flows. These results are consistent with previous observations in conventional no-slip flows (Mack 1984). To further investigate the impact of the slip wall on the oblique first- and second-mode waves, Figure 10 illustrates the growth rate of 3D mode S with different wave angles at $x^* = 0.746$ m for no-slip and slip cases. It can be observed that the slip effect decreases the maximum growth rate of the oblique second mode, while increasing the maximum growth rate of the oblique first mode. This observation aligns with the finding obtained for 2D waves.

Figure 11(a) depicts the impact of slip boundary on the neutral stability curves for the 2D mode S. As

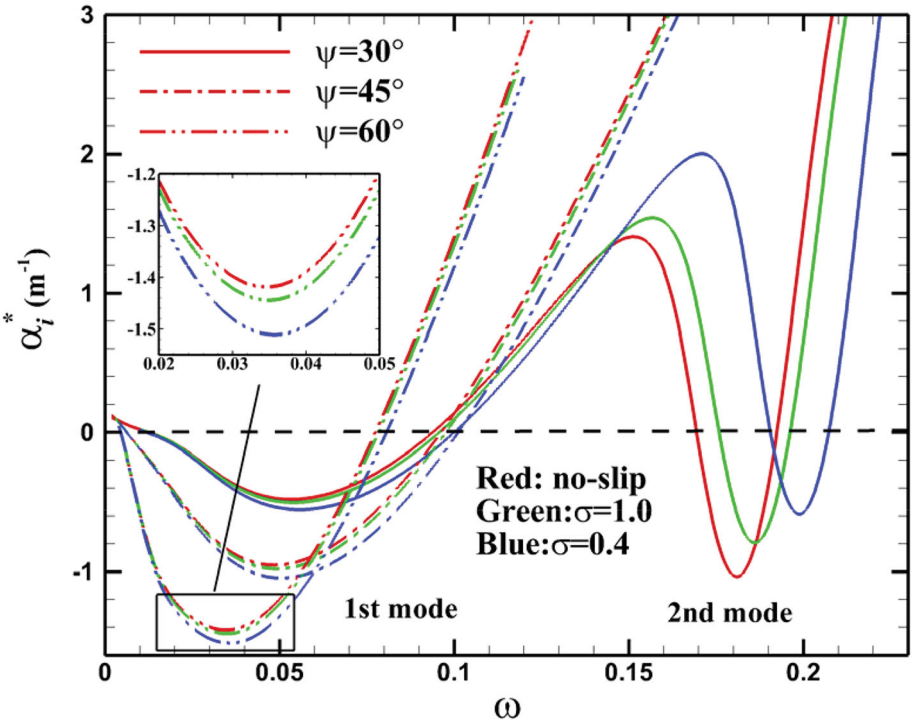

Figure 10. The variation of the growth rate with angular frequency at $x^* = 0.746$ m for three-dimensional mode S waves at various wave angles in the no-slip and different slip flows.

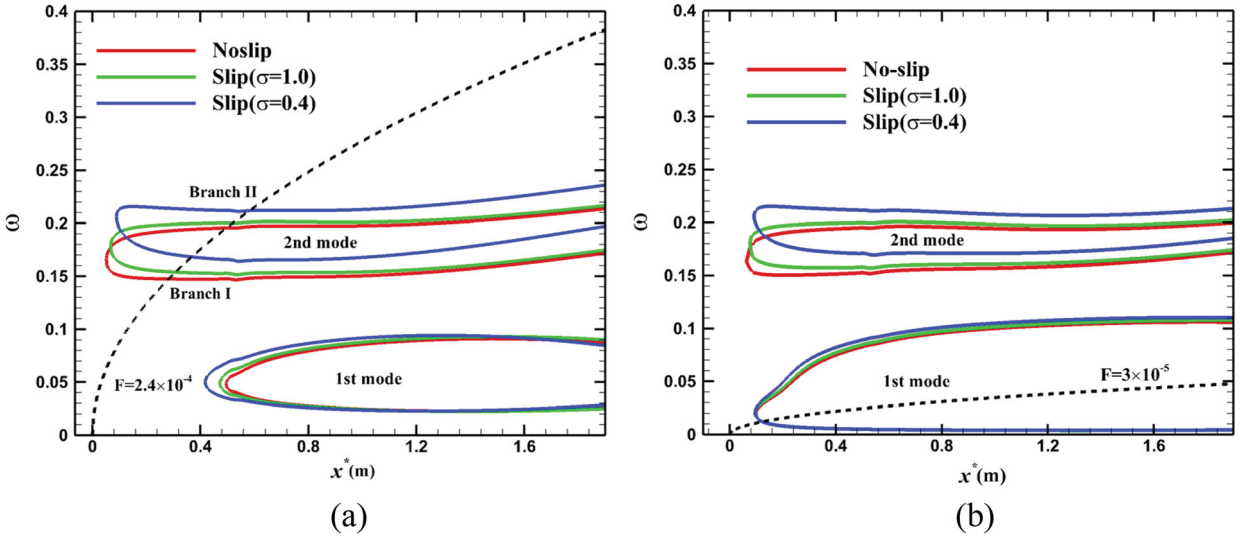

Figure 11. The neutral stability curves of (a) two-dimensional mode S and (b) three-dimensional mode S ($\beta^* = 85$ m^{-1}) for the no-slip and slip flows.

the slip effect becomes more significant, the occurrence of unstable first mode shifts upstream and the first-mode unstable region expands. In contrast, the second-mode unstable region is delayed downstream in slip flows, which is caused by the delayed synchronisation between mode S and mode F_1 (Figure 5). For oblique mode S waves, the slip boundary exhibits similar impacts on their neutral stability curves, as presented in Figure 11(b). However, the first-mode unstable region only experiences a slight upstream shift due to the slip effect.

According to LST, disturbances keep growing within their unstable region. At a specific streamwise location x^*, the amplification factor of the disturbance

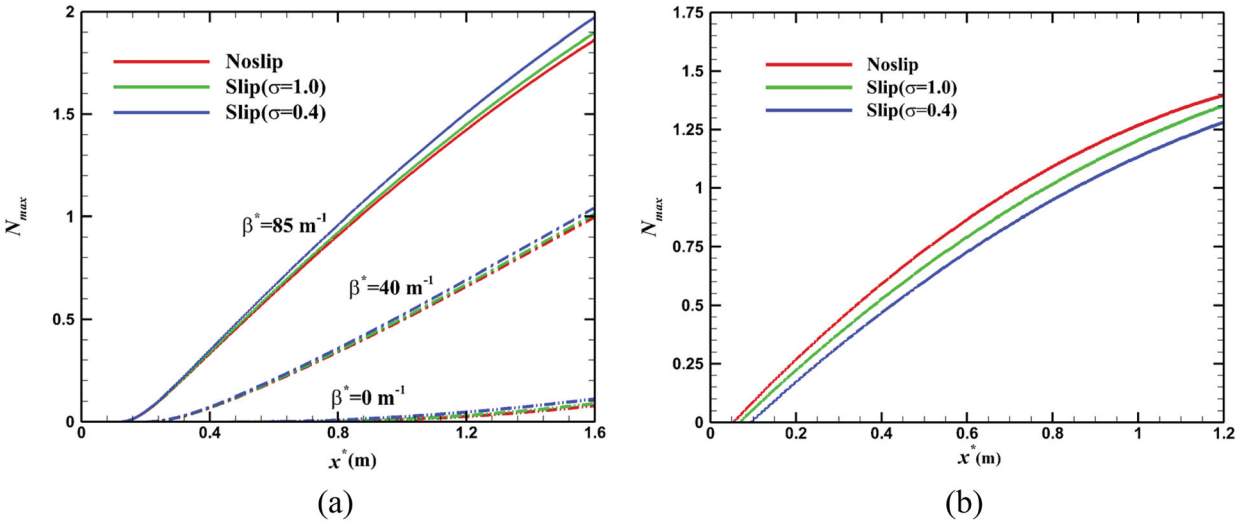

Figure 12. The maximum *N*-factor distribution of different frequency disturbances for (a) three-dimensional first mode and (b) two-dimensional second mode.

is usually defined as.

$$N(f^*, x^*) = \int_{x_0^*}^{x^*} -\alpha_i^* \mathrm{d}x^*, \tag{19}$$

where f^* denotes a specific frequency, and x_0^* corresponds to the location where the disturbance initially enters the unstable region. To examine the slip effect on the integral growth of the unstable first and second modes, the streamwise distribution of maximum N factor for mode S in no-slip and slip cases is given in Figure 12. Here, the maximum N is determined by obtaining the envelope of the N factor curves for disturbances at different frequencies. As depicted in Figure 12(a), the slip effect enhances the growth of the first mode with various spanwise wavenumbers. In contrast, Figure 12(b) illustrates that the second-mode growth is suppressed due to the slip boundary. This could be attributed to the fact that the slip wall decreases the second-mode local growth rate and delays the onset of the second-mode instability. These results further confirm that the slip boundary destabilises the first mode while stabilising the second mode. They also indicate that the slip wall could be detrimental to the low-Mach supersonic boundary-layer transition triggered by the first-mode waves, which are typically the dominant instability under this circumstance (Mack 1984).

3.2. Unsteady Simulations

Unsteady simulations are carried out to study the slip effect on the spatial evolution of boundary-layer waves. To quantify the magnitude of disturbances, unsteady computations have been conducted for one more period of time after numerical solutions have reached a periodic state. For 2D simulations, the Fourier transform is applied to the instantaneous pressure perturbation p' in the time direction, which leads to.

$$p'(x, y, t) = |p'(x, y)| \exp[i\,(\psi'(x, y) - \omega t)]\,. \tag{20}$$

For 3D simulations, the Fourier transform is performed in both the time and spanwise directions, which leads to

$$p'(x, y, z, t) = |p'(x, y)| \exp[i\,(\psi'(x, y) - \omega t - \beta z)]\,, \tag{21}$$

where $|p'|$ and ψ' are pressure perturbation amplitude and phase angle, respectively. The local wavenumber α^* related to pressure disturbances can be extracted in DNS as

$$\alpha_r{}^* = d|\psi'|/dx^*, \tag{22}$$

$$\alpha_i{}^* = -d|p'|/(|p'|dx). \tag{23}$$

It should be noted that $\alpha_r{}^*$ and $\alpha_i{}^*$ computed above represent the true wavenumber only when the disturbance is dominated by a single mode. Otherwise, both parameters are a result of the modulation of multiple mode waves in the flow field (Tumin, Wang, and Zhong 2007).

(1) *Spatial development of slow mode waves*

This section focuses on the impact of slip wall on the spatial evolution of mode S. Disturbances of mode

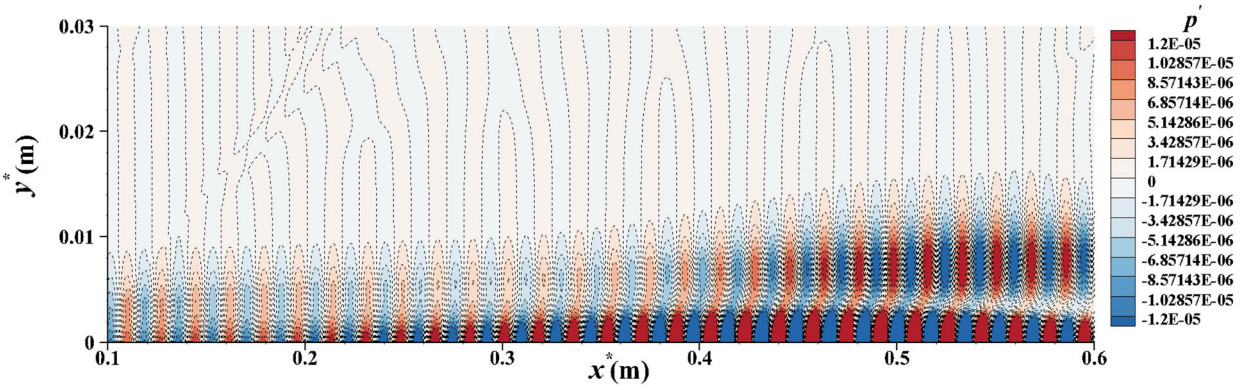

Figure 13. The contour of instantaneous pressure perturbation in the no-slip case.

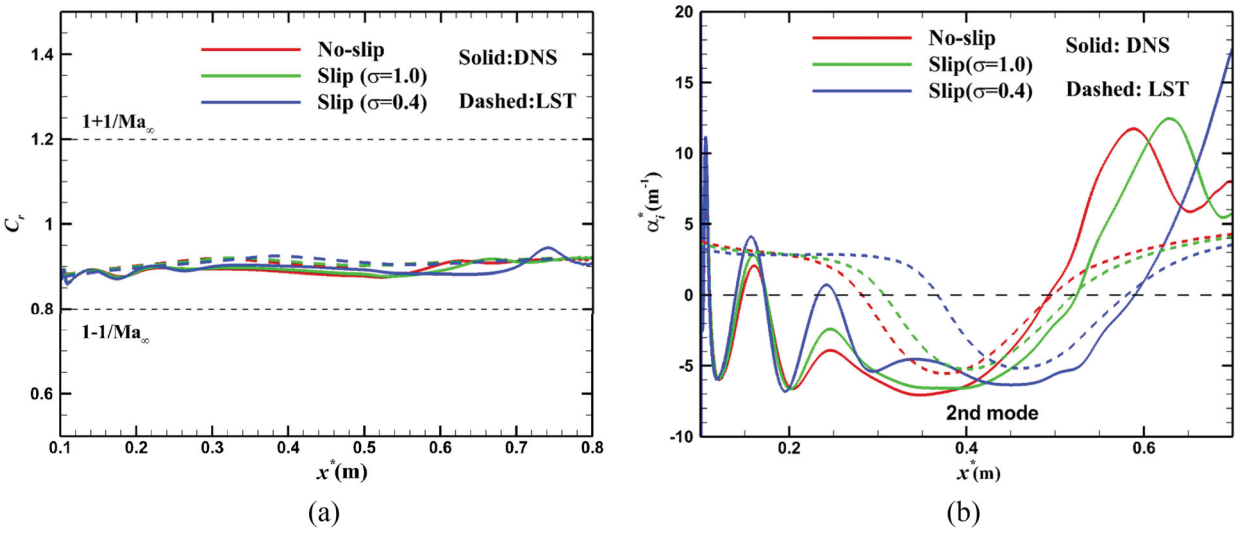

Figure 14. Comparison of the (a) phase velocities and (b) growth rates obtained from numerical simulations with those of mode S predicted by LST in the no-slip and slip cases.

S at a fixed frequency of $F = 2.4 \times 10^{-4}$ are introduced at $x^*_{\text{inlet}} = 0.1$ m for no-slip and slip cases. As the disturbances propagate downstream, they would pass through an unstable region of the second mode (Figure 11(a)). For instance, the contour of instantaneous pressure perturbation in the no-slip case is depicted in Figure 13. It reveals that two-cell structures are formed downstream with a longitudinal wave-length roughly twice the boundary-layer thickness, which is typical for the second-mode instability (Egorov, Fedorov, and Soudakov 2006).

Figure 14 compares the phase velocities and the growth rates obtained from DNS by Equations (22) and (23) with those of mode S predicted by LST in no-slip and slip cases. For a certain no-slip or slip case, the phase velocities obtained from numerical simulations agree well with those of mode S computed by LST as shown in Figure 14(a). Simultaneously, Figure 14(b) shows that the streamwise locations of maximum growth rate and branch II neutral stability point obtained from DNS are very close to those predicted by LST. However, there are some differences in results between DNS and LST. Particularly, the growth rate of mode S in the unstable region obtained by LST is slightly lower than DNS. In the downstream region, mode S obtained by DNS are more stable than that predicted by LST. These behaviours are also found in previous investigations for compressible boundary-layer stability (Ma and Zhong 2003a; Wang and Zhong 2012; Husmeier, Mayer, and Fasel 2005) and are attributed to the nonparallel flow effects. This statement gets further corroborated by the study involving nonlinear Parabolic Stability Equations (PSE) method (Mayer, Von Terzi, and Fasel 2008). In addition, the DNS results in Figure 14 exhibit some oscillations. These oscillations are a result of the coexistence of multiple

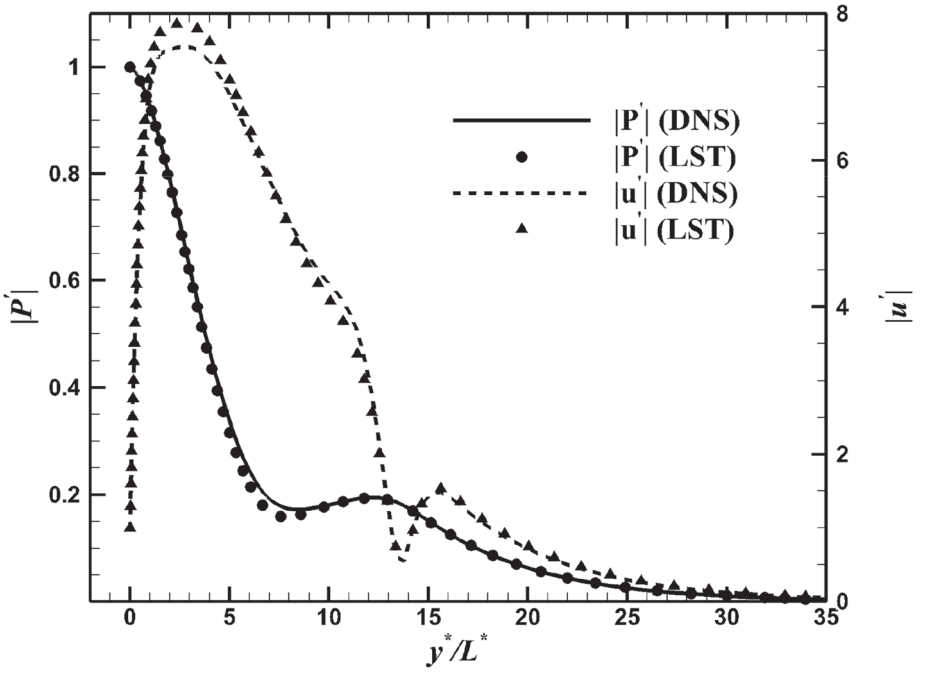

Figure 15. The eigenfunctions of temperature and streamwise velocity at $x^* = 0.4$ m obtained from DNS and those of mode S predicted by LST in the slip case ($\sigma = 1.0$).

mode waves in the flow filed (Ma and Zhong 2003a; Knisely and Zhong 2019b; Wang, Zhong, and Ma 2011; Zhao et al. 2018). As mentioned previously, the inlet-imposed waves are obtained from LST. Due to the nonparallel effects, these waves are only dominated by mode S or mode F in unsteady simulations. Furthermore, the modulation between different waves would enhance such oscillations. When mode S grows rapidly in the unstable region, other minor waves would have little impacts and thus the oscillations disappear. Whereas there are no oscillations in the LST results since LST neglects the modal interactions and only considers a single mode at one time. It should be noted that the influence of shock wave is negligible since mode S waves are confined within the boundary layer.

The DNS results indicate that the slip effect decreases the maximum growth rate in the unstable region, thus stabilising the second mode, and increases the second-mode most unstable frequency. However, the phase velocity of mode S is almost unaffected by the slip wall. These findings are consistent with the LST analysis. Overall, there is a good agreement in the wavenumber of mode S between DNS and LST. Such agreement is also observed when comparing the eigenfunction profiles, as illustrated in Figure 15.

The amplitudes of pressure perturbation along the wall in no-slip and slip cases are presented in Figure 16. It shows that the amplitude of pressure disturbance increases rapidly as the mode S wave in these cases enters its unstable zone, i.e. the second-mode region. It is apparent that the locations of maximum perturbation amplitudes obtained from DNS are nearly the same as those predicted by LST. Further downstream, the disturbance rapidly decays as mode S becomes stable. By comparison, the behaviour of exponential growth and the location of peak amplitude in slip flow are both delayed downstream when compared to the no-slip flow. This tendency gets more pronounced as σ lowers, proving that the second-mode unstable region indeed shifts downstream due to the slip effect.

In addition, it is noted that the maximum of pressure perturbation is increased in slip cases. This seems to contradict the conclusion that the slip effect stabilises the second mode. As mentioned previously, the amplitude of pressure perturbation $|p'|$ varying with streamwise location x^* can be calculated by integrating the growth rate $-\alpha_i^*$ along the streamwise direction as,

$$|p'(x^*)| = |p'_0|\exp\left(\int_{x_0^*}^{x^*} -\alpha_i^*(x^*)dx^*\right), \qquad (24)$$

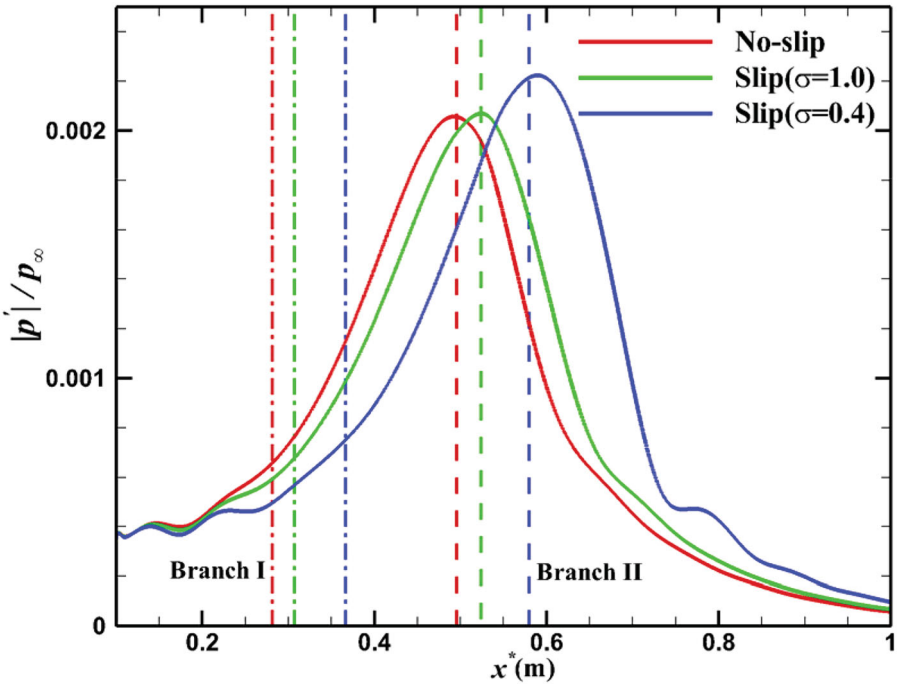

Figure 16. Comparison of the amplitudes of pressure perturbation along the wall for no-slip and slip cases. (Solid lines: the amplitude of pressure perturbation; vertical dash dot lines: branch I neutral stability points predicted by LST; vertical dashed lines: branch II neutral stability points predicted by LST.)

where $|p'_0|$ is the initial amplitude pressure perturbation at branch I neutral stability point, and x_0^* denotes the location of branch I neutral stability point. This equation illustrates that the maximum pressure perturbation $|p'_m|$ at branch II neutral stability point depends on three factors, i.e. the growth rate, the integration range and the initial amplitude. Among them, the initial amplitude of perturbation cannot be predicted by LST. Before mode S reaches the unstable region, there are oscillations in the perturbation amplitude. Additionally, the second-mode unstable region is delayed downstream by the slip effect. Thus, $|p'_0|$ is different for each no-slip and slip case. This might be the main reason for the increased maximum perturbation amplitude in slip flows. To support this deduction, Table 2 presents the amplitude of the initial pressure perturbation (at branch I neutral stability point) and the maximum pressure perturbation for no-slip and slip cases in Figure 16. It is found that $|p'_m|/|p'_0|$ is 3.135 for the no-slip case, 3.049 for the slip case ($\sigma = 1.0$) and 2.952 for the slip case ($\sigma = 0.4$). Given that the length of unstable region is almost unaffected by the slip wall, the present results indicate that the slip boundary does decrease the second-mode growth rate, i.e. the slip effect stabilises the second mode. Here, the locations of branch I neutral stability points predicted by LST are used as the reference since they are hard to be recognised from DNS due to the oscillations. Therefore, the increased $|p'_m|$ in slip cases is caused by the increased $|p'_0|$, which is due to the oscillations before the unstable region. However, the behaviours out of the unstable region are not the focus in this section.

Table 2. The amplitude of pressure perturbation at branch I neutral stability point and maximum pressure perturbation for no-slip and slip cases in Figure 12.

Cases	$\lvert p'_0\rvert/p_\infty$	$\lvert p'_m\rvert/p_\infty$	$\lvert p'_m\rvert/\lvert p'_0\rvert$
No-slip	0.000657	0.00206	3.135
Slip ($\sigma = 1.0$)	0.000679	0.00207	3.049
Slip ($\sigma = 0.4$)	0.000752	0.00222	2.952

To investigate the spatial development of oblique first-mode waves under the slip effect, disturbances of oblique mode S with the spanwise wavenumber of $\beta^* = 85\ \mathrm{m}^{-1}$ and a low frequency of $F = 3 \times 10^{-5}$ are imposed at the inlet of $x^* = 0.1$ m. Here, the 3D DNS is conducted to simulate the streamwise evolution of these oblique waves. As illustrated in Figure 11(b), the imposed oblique mode S waves would go through an unstable region of the first mode within the current computational domain. Figure 17 shows the streamwise evolution of pressure perturbation for

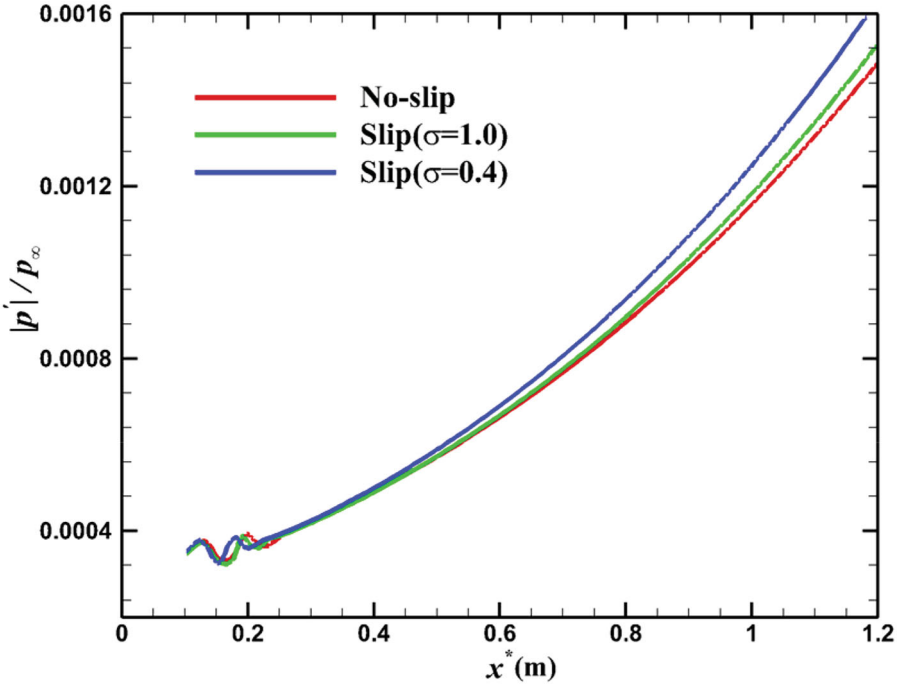

Figure 17. Comparison of the amplitudes of pressure perturbation along the wall for no-slip and slip cases with oblique mode S imposed at the inlet.

oblique mode S at the wall in the no-slip and different slip cases. It is evident that amplitude of pressure perturbation in each case grows continuously due to the first-mode instability. Upon comparison, it can be observed that the amplitude of pressure perturbation is getting larger as the slip effect becomes more pronounced. This suggests that the growth of the first mode is enhanced by the presence of slip boundary. In other words, the first mode is destabilised by the slip velocity and temperature jump, which is consistent with the previous LST analysis.

(2) *Spatial development of fast mode waves*

It is well-known that fast mode waves play a critical role in the receptivity process through their resonant interactions with fast acoustic waves and slow mode waves (Ma and Zhong 2003a; 2003b). Thus, it is necessary to use DNS to explore the impact of slip boundary on the spatial development of fast mode waves.

(a) *Mode F_1*. The slip effect on the spatial evolution of mode F_1 waves is first studied. Disturbances of mode F_1 at a frequency of $F = 2.4 \times 10^{-4}$ are imposed at the inlet of $x^* = 0.1$ m in no-slip and slip cases. Figure 18 shows the wall distribution of phase velocities obtained from DNS with those of mode F_1 and mode S predicted by LST. In the upstream region, the phase velocities obtained from DNS agree well with those of mode F_1 predicted by LST for each case. However, mode F_1 converts to mode S as propagating downstream. As shown in Figure 5, mode F_1 and mode S become synchronised at their synchronisation point, where both mode F_1 and mode S have almost the same profiles of disturbances across the boundary layer (Figure 6). Thus, due to their interactions, there occurs the conversion of mode F_1 to mode S as mode F_1 propagates to the region near their synchronisation. However, this conversion is not captured by LST (Figure 5) because LST can only track the single-mode wave and cannot resolve the resonant interactions between waves. Further downstream, the oscillations are also caused by the mixture of the induced mode S and other waves in the flow field. From Figure 18, it is evident that the synchronisation region where mode F_1 changes to mode S shifts downstream under the slip effect. This is because, in slip flows, the phase velocities of mode F_1 decay slower, whereas those of mode S are almost unaltered as shown in Figure 14(a).

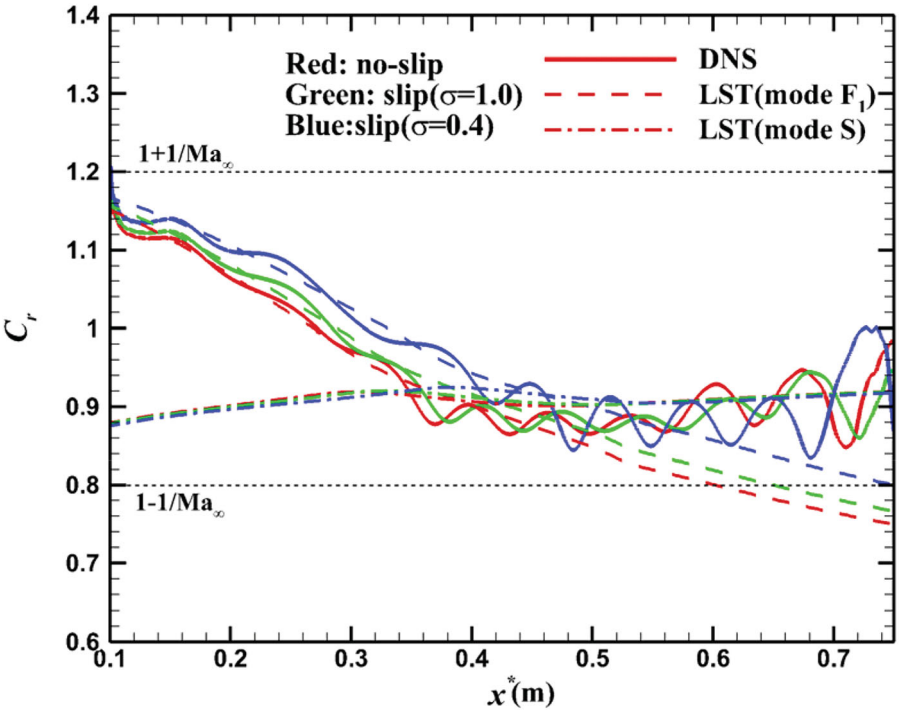

Figure 18. Comparison of the phase velocities obtained from DNS with those of mode F_1 and mode S predicted by LST for no-slip and slip cases.

The amplitudes of pressure perturbations along the wall in no-slip and slip cases are compared in Figure 19. It shows that the amplitude of pressure perturbation grows to its first peak downstream the inlet, which appears to contradict the LST prediction that fast mode waves are always stable (Figure 8). The same mechanism is also observed in a previous DNS study by Ma and Zhong (2003a) that investigated the propagations of fast mode waves in a no-slip flow. According to the previous study, this non-modal growth is attributed to the resonant interactions between mode F_1 and fast acoustic waves as mode F_1 is introduced near its synchronisation region with fast acoustic waves. Correspondingly, the waves begin to decay due to the inherent stability of mode F_1 when they move away from the synchronisation region. Further downstream, as mode F_1 converts to mode S after its synchronisation with mode S, the induced Mack instability causes the second growth for the perturbation. This is also confirmed in Figure 19, which shows that the location of the second peak of perturbation amplitude in each case is close to the second-mode branch II neutral stability points predicted by LST. In addition, the starting location of the second growth for the amplitude moves downstream as σ decreases, indicating the delayed conversion from mode F_1 to mode S under the slip effect. It should be noted that these amplifications of the perturbation are not led by the shock wave. Moreover, Figure 19 shows that the first amplification of the perturbation becomes more significant as the slip effect increases. It implies that the slip wall might strengthen the resonant interaction between mode F_1 and fast acoustic waves. Similarly, the oscillations in the results are due to the influence of multiple modes.

The instantaneous contours of disturbance energy $k' = (u')^2 + (v')^2$ for no-slip and slip cases are given in Figure 20. It depicts that the disturbance energy behind the inlet quickly amplifies due to the resonant interaction between mode F_1 and fast acoustic waves. Then, the disturbance energy decays downstream due to the inherent stability of mode F_1. The maximum disturbance energy in the flow field increases as σ decreases, indicating the enhanced resonance of mode F_1 and fast acoustic waves. According to the LST results, the slip wall enlarges the magnitudes of mode F_1 eigenfunctions, which might explain the enhancement of the resonant interactions. Figure 21 compares the eigenfunctions obtained from DNS and those of mode F_1 predicted by LST in no-slip and slip cases. Given the nonparallel-flow effects, the profiles of eigenfunction obtained from DNS agree well with

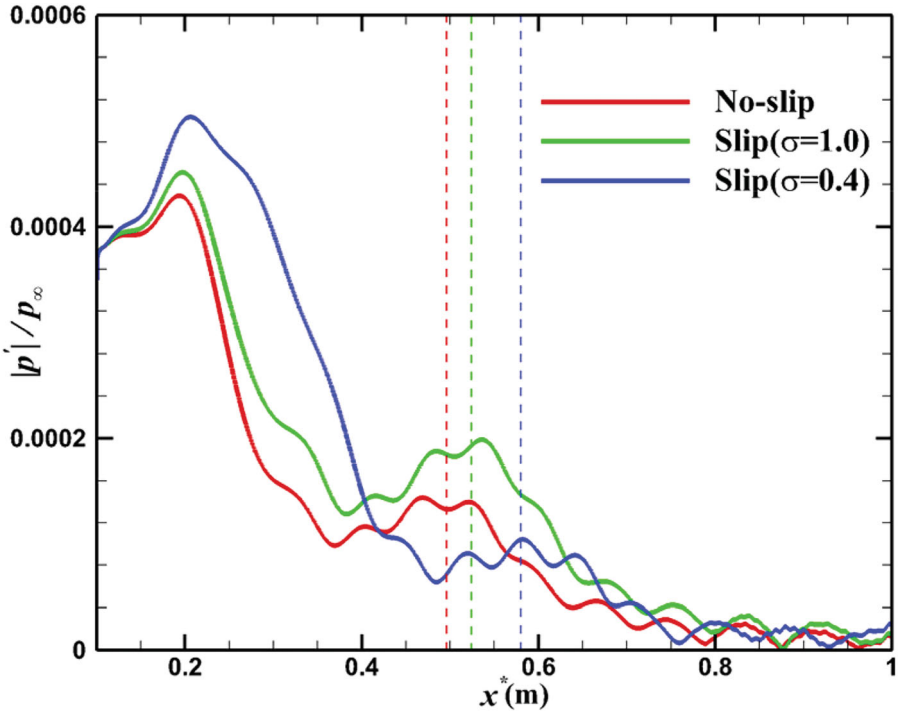

Figure 19. Comparisons of amplitudes of pressure perturbations along the wall for no-slip and slip cases. (Vertical dashed lines: branch II neutral stability points predicted by LST.)

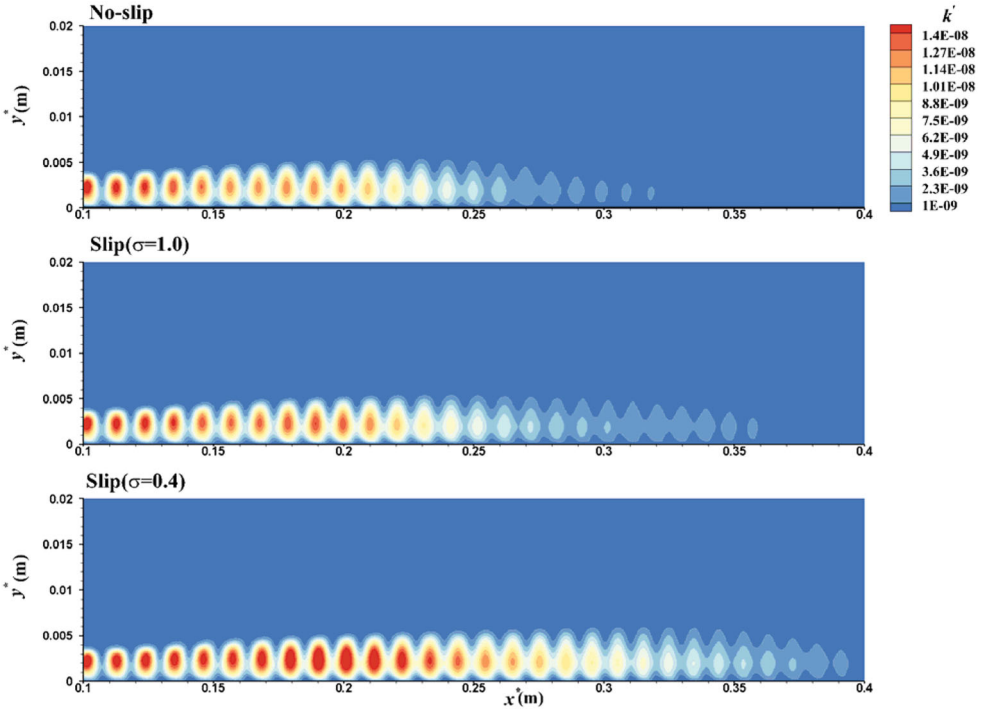

Figure 20. Instantaneous contours of disturbance energy in no-slip and slip flows for the cases of introduced mode F_1.

those predicted by LST. From this figure, the magnitudes of mode F_1 waves are indeed increased under the slip effect. Thus, the energy of mode F_1 waves increases under the slip effect, which strengthens their resonance with fast acoustic waves.

(b) *Mode F_2*. In this section, the disturbances of mode F_2 at the frequency of $F = 2.4 \times 10^{-4}$ are introduced at the inlet of $x^* = 0.72$ m in no-slip and slip cases. According to the LST results, this inlet is very close to the location where mode F_2 first

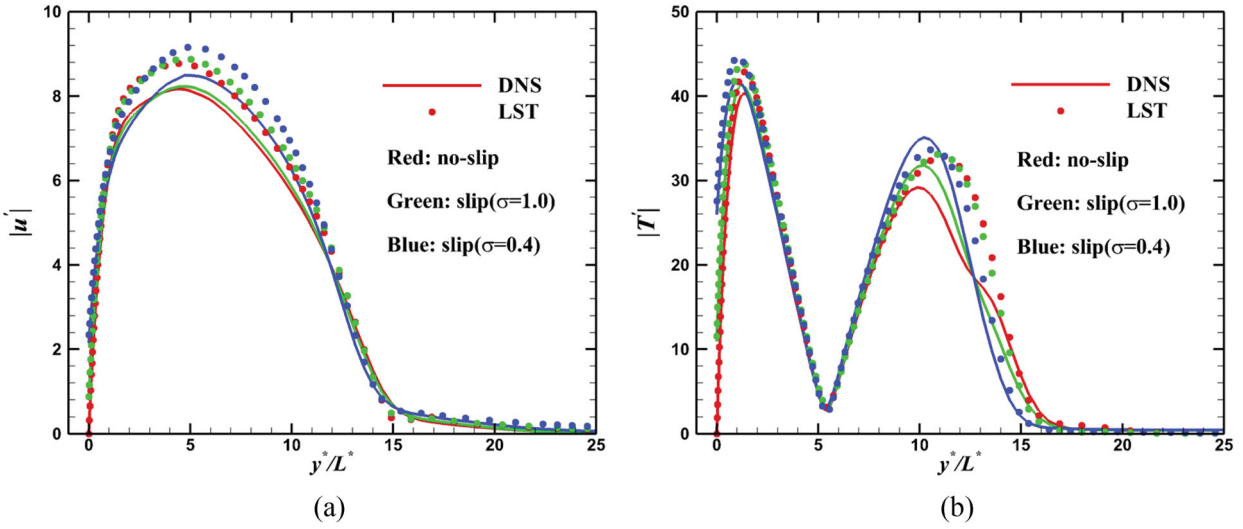

Figure 21. Eigenfunctions for (a) streamwise velocity and (b) temperature at $x^* = 0.25$ m obtained by numerical simulations and those of mode F_1 predicted by LST in no-slip and slip cases.

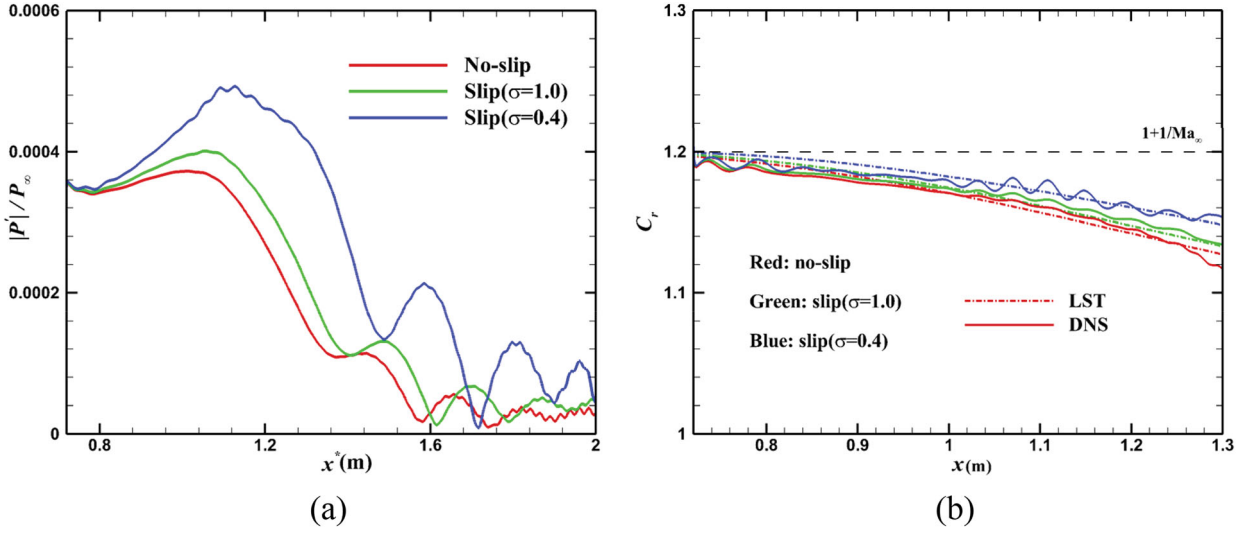

Figure 22. (a) The wall distributions of the amplitude of pressure perturbations for the no-slip and slip cases of imposed mode F_2 at the inlet of $x^* = 0.72$ m. (b) The comparison of phase velocities obtained from DNS with those of mode F_2 predicted by LST for the no-slip and slip cases of imposed mode F_2 at the inlet of $x^* = 0.72$ m.

appears, i.e. the synchronisation points of mode F_2 and fast acoustic waves.

Figure 22(a) shows the distribution of the amplitudes of pressure perturbations along the wall in no-slip and slip cases. The propagation profiles of current cases present several peaks in perturbation amplitudes due to a mixture of several modes. Particularly, despite LST predicting that mode F_2 is stable (Figure 8(a)), the amplitude of pressure perturbations grows rapidly to the first peak behind the inlet. Similar to the cases of imposed mode F_1 waves, this non-modal growth of the amplitude for perturbation is led by resonant interactions between mode F_2 and fast acoustic waves. This is because that the imposed mode F_2 waves synchronise with fast acoustic waves near the inlet. Meanwhile, the results in Figure 22(b) also reveal that mode F_2 waves are modulated by the fast acoustic waves due to their interactions.

The above statements can be also supported by Figure 23. Firstly, Figure 23(a) shows the wall distribution of the magnitudes of pressure perturbations in the no-slip and slip cases where the inlet of mode F_2 is fixed at $x^* = 1.0$ m. This inlet is far downstream

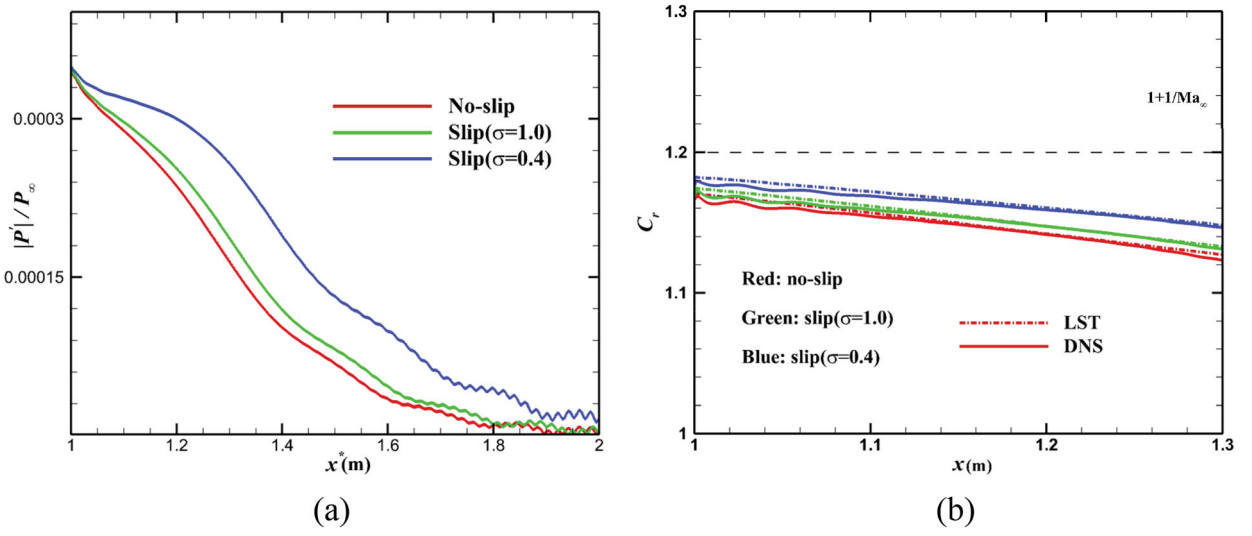

Figure 23. (a) The wall distributions of the amplitude of pressure perturbations for the no-slip and slip cases of imposed mode F_2 at the inlet of $x^* = 1.0$ m. (b) The comparison of phase velocities obtained from DNS with those of mode F_2 predicted by LST for the no-slip and slip cases of imposed mode F_2 at the inlet of $x^* = 1.0$ m.

the synchronisation point between fast acoustics waves and mode F_2. Unlike those shown in Figure 22(a), the amplitudes of pressure perturbation for no-slip and slip cases in Figure 23(a) are continuously decaying due to the stability of mode F_2, and there is no growth in the perturbation amplitude. This is because there are no interactions between mode F_2 and fast acoustic waves, as mode F_2 do not synchronise with fast acoustic waves in these cases. Correspondingly, the phase velocities obtained from DNS agree very well with those of LST, as shown in Figure 23(b). Additionally, Figure 23(a) clearly shows that the decay rate of mode F_2 is decreased by the slip boundary, which is consistent with the LST analysis (Figure 8(a)). Back to Figure 22(a), the first peak of perturbation amplitude rises as the slip effect increases. This indicates the enhanced resonance between mode F_2 waves and fast acoustic waves. Then, downstream from the first peak of the perturbation amplitude, the inherent stability of mode F_2 leads to the decay of the perturbation amplitude.

Figure 24 shows the instantaneous contour of disturbance energy in the no-slip and slip cases of imposed mode F_2 at the inlet of $x^* = 0.72$ m. Due to the interactions between mode F_2 and fast acoustic waves, the disturbance energy gradually increases in the upstream region. Different from the field of disturbance energy for mode F_1, two-cell structures are formed in the field of disturbance energy for mode F_2. This is because that the eigenfunction of velocity for mode F_2 has two peaks, whereas there is only one peak in the eigenfunction of velocity for mode F_1 (Figure 7). In Figure 24, the maximum disturbance energy increases as σ decreases, also indicating the enhanced resonant interactions between mode F_2 and fast acoustic waves. As mode F_2 waves resonate with fast acoustic waves mainly outside the boundary layer (Ma and Zhong 2003a), the eigenfunction profiles at $x^* = 0.9$ m obtained from DNS and those of mode F_2 predicted by LST are compared in Figure 25. The figure exhibits good agreements in wave structures inside the boundary layer between the results of DNS and LST, demonstrating the dominance of mode F_2 in this area. However, two sets of results present major differences outside the boundary layer since the resonance cannot be captured by LST. It is clear that the slip effect increases the eigenfunction magnitudes of mode F_2, especially outside the boundary layer. Thereby, the resonant interactions between mode F_2 and fast acoustic waves are enhanced.

It should be noted that the above results still hold true when the frequency of imposed disturbance is altered. In summary, the impacts of slip boundary on the modal stability and the resonances between fast acoustic waves, fast mode waves and slow mode waves are studied by comparing the spatial development of the fast and slow mode waves in no-slip and slip cases. On the one hand, it is found the impacts of slip boundary on the stability of boundary-layer waves obtained from DNS are consistent with those predicted by LST. On the other hand, the modal resonant interactions

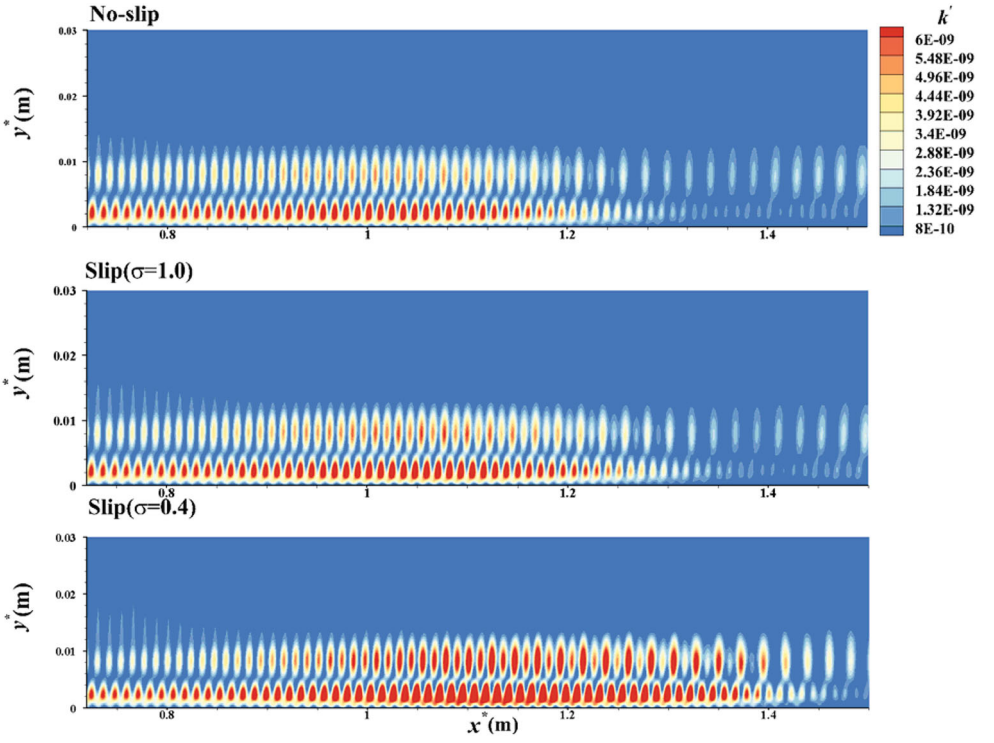

Figure 24. The instantaneous contours of disturbance energy in no-slip and slip cases of imposed mode F_2 at the inlet of $x^* = 0.72$ m.

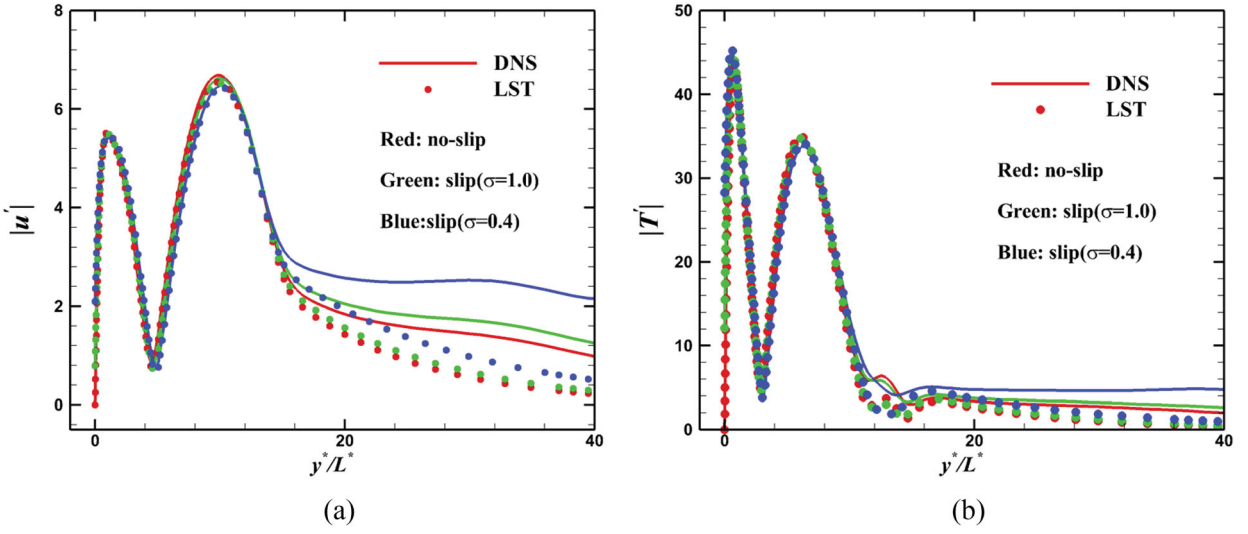

Figure 25. Comparison of the eigenfunctions of mode F_2 obtained by LST and unsteady simulations at $x^* = 0.9$ m in no-slip and slip case where the mode F_2 waves are imposed at the inlet of $x^* = 0.72$ m.

that cannot be resolved by LST are also studied. Most importantly, the present result reveals that the slip boundary can strengthen the resonant interactions between fast mode waves and fast acoustic waves.

4. Conclusions

Within the NS framework, DNS and LST are both used to study the linear stability and resonant interactions of boundary-layer waves for a Mach 5 flat plate in the slip regime. The slip velocity and temperature jump are modelled by the M-S slip boundary conditions. The NS equations with no-slip and slip boundary conditions are numerically solved to obtain steady and unsteady flow fields with different degrees of the slip effect. Moreover, the LST that considers wall perturbation boundary conditions for no-slip and slip flows is adopted.

Based on the steady solutions, the slip effect on the modal stability is first analysed by LST. Fast mode waves are found to remain stable in slip flows but their decay rates are lower than those in no-slip flows. Regarding the mode S, it constitutes both the first mode and second mode of Mack in current cases. In slip flows, the 2D instability is dominant for the second mode, while the 3D instability is dominant for the first mode. The analyses of the local growth rate and the integrated N factor both suggest that the slip velocity and temperature jump tend to stabilise the second mode but destabilise the first mode. Additionally, the synchronisation process of fast and slow modes is studied. The slip effect causes the phase velocity of fast mode to decrease more slowly while having little impacts on that of mode S, which leads to the delayed synchronisation between fast modes and mode S. Correspondingly, the onset of second-mode instability is delayed downstream in the slip flow. However, the first-mode unstable region gets enlarged and moves upstream under the influence of slip wall.

Subsequently, unsteady simulations are carried out to study the spatial development of mode F_1, F_2 and S waves under different degrees of slip effect. The results show that the phase velocity, the growth rate and the eigenfunction obtained from DNS agree well with those predicted by LST, except for the discrepancy mainly caused by nonparallel flow effects. Furthermore, the unsteady DNS results also reveal that the slip effect enhances the streamwise growth of the first mode, while suppressing the second-mode streamwise growth. Accordingly, the impacts of the slip wall on the linear stability characteristics of fast and slow modes, as predicted by LST, have been confirmed through DNS. Also, the developed LST method for analysing slip flow has been validated. Moreover, the resonant interactions between boundary-layer waves that cannot be resolved in LST are also studied by unsteady simulations. The numerical results demonstrate that the slip boundary indeed postpones the resonance between mode S and mode F_1, through which mode F_1 converts to mode S. Additionally, the interactions between fast acoustic waves and mode F_1 and F_2 lead to the amplification of mode F_1 and F_2 waves, even though both of them are predicted to be stable by LST. This non-modal amplification of fast mode waves becomes more significant due to the slip effect, indicating enhanced resonant interactions between fast mode and fast acoustic waves. This phenomenon can be attributed to the increased magnitude of the eigenfunction of fast modes.

This work sheds a light on the study of high-speed boundary-layer stability and transition with local slip effects using both numerical and theoretical methods. However, further research on the receptivity process affected by the free-stream rarefaction effects is needed to fully understand the relevant mechanisms.

Acknowledgements

The authors are grateful to Prof. Xinliang Li from the University of Chinese Academy of Sciences, for the high-order finite-difference solver.

Disclosure statement

No potential conflict of interest was reported by the author(s).

Funding

This research was supported by the National Natural Science Foundation of China (NSFC grant numbers 12002306, 92271204, and U20B2007).

Data Availability

The data that support the findings of this study are available from the corresponding author upon reasonable request.

ORCID

Lun Zhang http://orcid.org/0000-0002-0015-8903
Zhongzheng Jiang http://orcid.org/0000-0002-3151-0076

References

Abu Rowin, W., J. Hou, and S. Ghaemi. 2017. "Inner and Outer Layer Turbulence Over a Superhydrophobic Surface with low Roughness Level at low Reynolds Number." *Physics of Fluids* 29: 095106. doi:10.1063/1.5004398

Ba, W., M. Niu, and C. Su. 2023. "Hypersonic Boundary-Layer Receptivity Over Circular Cones with Ellipsoidal/Spherical Noses." *AIAA Journal* 61: 518–533. doi:10.2514/1.J061846

Balakumar, P. and M. Kegerise. 2011. "Receptivity of Hypersonic Boundary Layers to Acoustic and Vortical Disturbances." AIAA Paper No. 2011-371.

Balakumar, P., R. A. King, A. Chou, L. R. Owens, and M. A. Kegerise. 2018. "Receptivity and Forced Response to Acoustic Disturbances in High-Speed Boundary Layers." *AIAA Journal* 56: 510–523. doi:10.2514/1.J056145

Boyd, I. D., G. Chen, and G. V. Candler. 1995. "Predicting Failure of the Continuum Fluid Equations in Transitional Hypersonic Flows." *Physics of Fluids* 7: 210–219. doi:10.1063/1.868720

Chai, C., and B. Song. 2019. "Stability of Slip Channel Flow Revisited." *Physics of Fluids* 31: 084105. doi:10.1063/1.5108804

Chen, Y., G. Tu, B. Wan, C. Su, X. Yuan, and J. Chen. 2021. "Receptivity of a Hypersonic Flow Over a Blunt Wedge to a Slow Acoustic Wave." *Physics of Fluids* 33: 084114. doi:10.1063/5.0062557

Choi, C.-H., K. J. A. Westin, and K. S. Breuer. 2003. "Apparent Slip Flows in Hydrophilic and Hydrophobic Microchannels." *Physics of Fluids* 15: 2897. doi:10.1063/1.1605425

Dash, S. and J. Papp. 2002. "Hypersonic Transitional Modeling for Scramjet and Missile Applications." AIAA Paper No. 2002-155.

Egorov, I. V., A. V. Fedorov, and V. G. Soudakov. 2006. "Direct Numerical Simulation of Disturbances Generated by Periodic Suction-Blowing in a Hypersonic Boundary Layer." *Theoretical and Computational Fluid Dynamics* 20: 41–54. doi:10.1007/s00162-005-0001-y

Fedorov, A. 2011. "Transition and Stability of High-Speed Boundary Layers." *Annual Review of Fluid Mechanics* 43: 79–95. doi:10.1146/annurev-fluid-122109-160750

Fedorov, A. V., and A. P. Khokhlov. 2001. "Prehistory of Instability in a Hypersonic Boundary Layer." *Theoretical and Computational Fluid Dynamics* 14: 359–375. doi:10.1007/s001620100038

Fedorov, A. V., and A. Tumin. 2011. "High-speed Boundary-Layer Instability: Old Terminology and a new Framework." *AIAA Journal* 49: 1647–1657. doi:10.2514/1.J050835

Graur, I. A., P. Perrier, W. Ghozlani, and J. G. Méolans. 2009. "Measurements of Tangential Momentum Accommodation Coefficient for Various Gases in Plane Microchannel." *Physics of Fluids* 21: 102004. doi:10.1063/1.3253696

Guo, Z., J. Li, and K. Xu, "Unified Preserving Properties of Kinetic Schemes," Physical Review E 107, 025301 (2023). doi:10.1103/PhysRevE.107.025301

Han, Y., and W. Cao. 2019. "Flat-plate Hypersonic Boundary-Layer Flow Instability and Transition Prediction Considering air Dissociation." *Applied Mathematics and Mechanics* 40: 719–736. doi:10.1007/s10483-019-2480-6

He, X., K. Zhang, and C. Cai. 2019. "Stability Analysis on Nonequilibrium Supersonic Boundary Layer Flow with Velocity-Slip Boundary Conditions." *Fluids* 4: 142. doi:10.3390/fluids4030142

He, S., and X. Zhong. 2021. "Hypersonic Boundary-Layer Receptivity Over a Blunt Cone to Freestream Pulse Disturbances." *AIAA Journal* 59: 3546–3565. doi:10.2514/1.J059697

Hollis, B. R. 2012. "Blunt-body Entry Vehicle Aerothermodynamics: Transition and Turbulent Heating." *Journal of Spacecraft and Rockets* 49: 435–449. doi:10.2514/1.51864

Horvath, T. J., J. N. Zalameda, W. A. Wood, S. A. Berry, R. J. Schwartz, R. F. Dantowitz, T. S. Spisz, and J. C. Taylor. 2012 April. "Global Infrared Observations of Roughness Induced Transition on the Space Shuttle Orbiter." Specialists' Meeting on Hypersonic Laminar-Turbulent Transition, Paper RTO, NASA AVT-200 RSM-030, NF1676L-13455.

Husmeier, F., C. Mayer, and H. Fasel. 2005. "Investigation of Transition of Supersonic Boundary Layers at Mach 3 Using DNS." AIAA Paper No. 2005-95.

Ivanov, M. S., and S. F. Gimelshein. 1998. "Computational Hypersonic Rarefied Flows." *Annual Review of Fluid Mechanics* 30: 469–505. doi:10.1146/annurev.fluid.30.1.469

Jiang, Z., W. Zhao, W. Chen, and Z. Yuan. 2021. "Eu's Generalized Hydrodynamics with its Derived Constitutive Model: Comparison to Grad's Method and Linear Stability Analysis." *Physics of Fluids* 33: 127116. doi:10.1063/5.0071715

Kara, K., P. Balakumar, and O. Kandil. 2007. "Receptivity of Hypersonic Boundary Layers Due to Acoustic Disturbances Over Blunt Cone." AIAA Paper No. 2007- 945.

Kara, K., P. Balakumar, and O. A. Kandil. 2011. "Effects of Nose Bluntness on Hypersonic Boundary-Layer Receptivity and Stability Over Cones." *AIAA Journal* 49: 2593–2606. doi:10.2514/1.J050032

Klothakis, A., H. Quintanilha, S. S. Sawant, E. Protopapadakis, V. Theofilis, and D. A. Levin. 2022. "Linear Stability Analysis of Hypersonic Boundary Layers Computed by a Kinetic Approach: A Semi-Infinite Flat Plate at $4.5 \leq M\infty \leq 9$." *Theoretical and Computational Fluid Dynamics* 36: 117–139. doi:10.1007/s00162-021-00601-y

Klothakis, A., S. S. Sawant, H. Quintanilha, V. Theofilis and D. A. Levin. 2021. "Slip Effects on the Stability of Supersonic Laminar Flat Plate Boundary Layer." AIAA Paper No. 2021-1659.

Knisely, C. P., and X. Zhong. 2019a. "Sound Radiation by Supersonic Unstable Modes in Hypersonic Blunt Cone Boundary Layers. I. Linear Stability Theory." *Physics of Fluids* 31: 024103. doi:10.1063/1.5055761

Knisely, C. P., and X. Zhong. 2019b. "Sound Radiation by Supersonic Unstable Modes in Hypersonic Blunt Cone Boundary Layers. II. Direct Numerical Simulation." *Physics of Fluids* 31: 024104. doi:10.1063/1.5077007

Li, X., D. Fu, and Y. Ma. 2010. "Direct Numerical Simulation of Hypersonic Boundary Layer Transition Over a Blunt Cone with a Small Angle of Attack." *Physics of Fluids* 22: 025105. doi:10.1063/1.3313933

Liang, X., and X. Li. 2013. "DNS of a Spatially Evolving Hypersonic Turbulent Boundary Layer at Mach 8." *Science China Physics, Mechanics and Astronomy* 56: 1408–1418. doi:10.1007/s11433-013-5102-9

Lin, T. C. 2008. "Influence of Laminar Boundary-Layer Transition on Entry Vehicle Designs." *Journal of Spacecraft and Rockets* 45: 165–175. doi:10.2514/1.30047

Liu, J., J. Xu, C. Wang, P. Yu, and J. Bai. 2021. "Pressure Gradient Effects on the Secondary Instability of Mack Mode Disturbances in Hypersonic Boundary Layers." *Physics of Fluids* 33: 014109. doi:10.1063/5.0033183

Liu, B., and Y. Zhang. 2020. "A Numerical Study on the Natural Transition Locations in the Flat-Plate Boundary Layers on Superhydrophobic Surfaces." *Physics of Fluids* 32: 124103. doi:10.1063/5.0030713

Ma, Y., and X. Zhong. 2003a. "Receptivity of a Supersonic Boundary Layer Over a Flat Plate. Part 1. Wave Structures

and Interactions." *Journal of Fluid Mechanics* 488: 31–78. doi:10.1017/S0022112003004786

Ma, Y., and X. Zhong. 2003b. "Receptivity of a Supersonic Boundary Layer Over a Flat Plate. Part 2. Receptivity to Free-Stream Sound." *Journal of Fluid Mechanics* 488: 79–121. doi:10.1017/S0022112003004798

Ma, Y., and X. Zhong. 2005. "Receptivity of a Supersonic Boundary Layer Over a Flat Plate. Part 3. Effects of Different Types of Free-Stream Disturbances." *Journal of Fluid Mechanics* 532: 63–109. doi:10.1017/S0022112005003836

Mack, L. M. 1975. "Linear Stability Theory and the Problem of Supersonic Boundary- Layer Transition." *AIAA Journal* 13: 278–289. doi:10.2514/3.49693

Mack, L. M. 1984. "Boundary-Layer Linear Stability Theory." Technical Report No. AGARD-R-709.

Malik, M. R. 1990. "Numerical Methods for Hypersonic Boundary Layer Stability." *Journal of Computational Physics* 86: 376–413. doi:10.1016/0021-9991(90)90106-B

Manela, A., and J. Zhang. 2012. "The Effect of Compressibility on the Stability of Wall-Bounded Kolmogorov Flow." *Journal of Fluid Mechanics* 694: 29–49. doi:10.1017/jfm.2011.499

Maxwell, J. C. 1879. "On Stresses in Rarified Gases Arising from Inequalities of Temperature." *Philosophical Transactions of the Royal Society of London* 27: 304–308.

Mayer, C., D. Von Terzi, and H. Fasel. 2008. "DNS of Complete Transition to Turbulence via Oblique Breakdown at Mach 3." AIAA Paper No. 2008-4398.

Moss, J. N., and G. A. Bird. 2003. "Direct Simulation of Transitional Flow for Hypersonic Reentry Conditions." *Journal of Spacecraft and Rockets* 40: 830–843. doi:10.2514/2.6909

Myong, R. S., and K. Xu. 2021. "Special Issue on Recent Hot Topics in Rarefied Gas Dynamics." *International Journal of Computational Fluid Dynamics* 35: 563–565. doi:10.1080/10618562.2021.2050478

Ou, J., and J. Chen. 2021. "Numerical Study of Supersonic Boundary-Layer Modal Stability for a Slightly Rarefied gas Using Navier-Stokes Approach." *Physics of Fluids* 33: 114107. doi:10.1063/5.0065283

Park, J., and D. Park. 2023. "Effects of Thermo-Chemical Models on Linear Stability Analysis of Chemically Reacting Hypersonic Boundary Layers." *International Journal of Aeronautical and Space Sciences*. 24: 985–1003. doi:10.1007/s42405-023-00614-3

Park, J., P. T. Rajendran, M. Kim, J. Lim, Jee S, Park D. 2023. "Effect of Local Thermal Strips on Hypersonic Boundary-Layer Instability." *Computers & Fluids* 257: 105868. doi:10.1016/j.compfluid.2023.105868

Qi, H., X. Li, C. Yu, and F. Tong. 2021. "Direct Numerical Simulation of Hypersonic Boundary Layer Transition Over a Lifting-Body Model HyTRV." *Advances in Aerodynamics* 3: 31. doi:10.1186/s42774-021-00082-x

Ragta, L. K., B. Srinivasan, and S. S. Sinha. 2017. "Efficient Simulation of Multidimensional Continuum and non-Continuum Flows by a Parallelised Unified gas Kinetic Scheme Solver." *International Journal of Computational Fluid Dynamics* 31: 292–309. doi:10.1080/10618562.2017.1350265

Reed, H. L., W. S. Saric, and D. Arnal. 1996. "Linear Stability Theory Applied to Boundary Layers." *Annual Review of Fluid Mechanics* 28: 389–428. doi:10.1146/annurev.fl.28.010196.002133

Samaha, M. A., and M. Gad-el Hak. 2021. "Slippery Surfaces: A Decade of Progress." *Physics of Fluids* 33: 071301. doi:10.1063/5.0056967

Sawant, S. S., V. Theofilis, and D. A. Levin. 2022. "On the Synchronisation of Three-Dimensional Shock Layer and Laminar Separation Bubble Instabilities in Hypersonic Flow Over a Double Wedge." *Journal of Fluid Mechanics* 941: A7. doi:10.1017/jfm.2022.276

Thompson, R., H. Hamilton, Ii, S. Berry, T. Horvath, and R. Nowak. 1998. "Hypersonic Boundary Layer Transition for X-33 Phase II Vehicle," AIAA Paper No. 1998-867.

Trott, W. M., J. N. Castañeda, J. R. Torczynski, M. A. Gallis, and D. J. Rader. 2011. "An Experimental Assembly for Precise Measurement of Thermal Accommodation Coefficients." *Review of Scientific Instruments* 82: 035120. doi:10.1063/1.3571269

Tumin, A., X. Wang, and X. Zhong. 2007. "Direct Numerical Simulation and the Theory of Receptivity in a Hypersonic Boundary Layer." *Physics of Fluids* 19: 014101. doi:10.1063/1.2409731

Tumuklu, O., D. A. Levin, and V. Theofilis. 2018. "Investigation of Unsteady, Hypersonic, Laminar Separated Flows Over a Double Cone Geometry Using a Kinetic Approach." *Physics of Fluids* 30: 046103. doi:10.1063/1.5022598

von Smoluchowski, M. 1898. "Ueber Wärmeleitung in verdünnten Gasen." *Annalen der Physik* 300: 101–130. doi:10.1002/andp.18983000110

Wan, B., J. Luo, and C. Su. 2018. "Response of a Hypersonic Blunt Cone Boundary Layer to Slow Acoustic Waves with Assessment of Various Routes of Receptivity." *Applied Mathematics and Mechanics* 39: 1643–1660. doi:10.1007/s10483-018-2391-6

Wan, B., C. Su, and J. Chen. 2020. "Receptivity of a Hypersonic Blunt Cone: Role of Disturbances in Entropy Layer." *AIAA Journal* 58: 4047–4054. doi:10.2514/1.J058816

Wang, X., and X. Zhong. 2012. "The Stabilization of a Hypersonic Boundary Layer Using Local Sections of Porous Coating." *Physics of Fluids* 24: 034105. doi:10.1063/1.3694808

Wang, X., X. Zhong, and Y. Ma. 2011. "Response of a Hypersonic Boundary Layer to Wall Blowing-Suction." *AIAA Journal* 49: 1336–1353. doi:10.2514/1.J050173

Yang, Z., S. Liu, C. Zhuo, and C. Zhong. 2022. "Conservative Multilevel Discrete Unified gas Kinetic Scheme for Modeling Multiphase Flows with Large Density Ratios." *Physics of Fluids* 34: 043316. doi:10.1063/5.0086723

Zhang, W.-M., G. Meng, and X. Wei. 2012. "A Review on Slip Models for gas Microflows." *Microfluidics and Nanofluidics* 13: 845–882. doi:10.1007/s10404-012-1012-9

Zhao, R., C. Y. Wen, X. D. Tian, T. H. Long, and W. Yuan. 2018. "Numerical Simulation of Local Wall Heating and

Cooling Effect on the Stability of a Hypersonic Boundary Layer." *International Journal of Heat and Mass Transfer* 121: 986–998. doi:10.1016/j.ijheatmasstransfer.2018.01.054

Zhong, X., R. W. MacCormack, and D. R. Chapman. 1993. "Stabilization of the Burnett Equations and Application to Hypersonic Flows." *AIAA Journal* 31: 1036–1043. doi:10.2514/3.11726

Zhong, X., and X. Wang. 2012. "Direct Numerical Simulation on the Receptivity, Instability, and Transition of Hypersonic Boundary Layers." *Annual Review of Fluid Mechanics* 44: 527–561. doi:10.1146/annurev-fluid-120710-101208

Appendix

Validation

A. DNS

To verify the accuracy of DNS, the present steady solutions for the no-slip case are first compared with a laminar compressible Blasius solution. As shown in Figure A1, the profiles of streamwise velocity and temperature obtained by DNS are consistent with the compressible Blasius solutions. Additionally, a case from Ou and Chen (2021) is taken as a reference benchmark to verify the DNS code with M-S slip boundary conditions. In this case, a flat-plate flow at Mach 4.5 in the slip regime is computed. Figure A2 compares the wall-normal profiles of streamwise velocity and temperature at $x^* = 0.5$ m, as well as the wall distribution of streamwise velocity and temperature computed by Ou and Chen (2021) and present code. The good agreement demonstrates the accuracy of present method.

In addition, the grid independence for steady and unsteady solutions of no-slip and slip cases are studied. From Figure A1, the numerical results based on two different grid resolutions agree well, proving the grid independence of current steady calculations. Meanwhile, Figure A3 shows the spatial evolution of mode S at the frequency of $F = 2.4 \times 10^{-4}$ in no-slip and slip cases obtained by unsteady simulations using the present and a higher grid resolution. It is obvious the present grid resolution is sufficient to accurately track the development of disturbances.

B. LST

The code of LST with both no-slip and slip wall perturbation boundary conditions is verified in this part. Firstly, the results of Ma and Zhong (Ma and Zhong 2003a) for the stability of a supersonic no-slip boundary layer are considered. The distributions of growth rates and phase velocities of various boundary-layer modes are calculated at a fixed streamwise location. Moreover, both adiabatic and isothermal wall conditions are employed as two bounds for temperature perturbations, which are denoted by $\partial\widehat{T}/\partial y|_{y=0} = 0$ and $\widehat{T}|_{y=0} = 0$, respectively. Figure A4 compares the results obtained by Ma and Zhong (2003a) and the present code. The excellent agreement proves the high accuracy of present LST for analysing no-slip flows.

Meanwhile, the results for a rarefied Mach 4.5 flat-plate boundary layer in Ref. 5 are used to examine the accuracy of our LST code with the slip-wall perturbation boundary conditions. As can be seen in Figure A5, the growth rate and the phase velocity versus frequency calculated by the present code and their counterparts in the reference are very close. Furthermore, we test the case in Klothakis et al. (2022), who obtained the modal eigenvalue of a supersonic laminar boundary layer corresponding to the altitude of 55 km using DSMC and LST. The eigenvalue of a temporal mode at $x^* = 0.7$ m obtained by Klothakis et al. (2022) and the present method is compared in the Table A1, and it is clear that both eigenvalues are very close. Thus, the reliability of our LST solver is fully verified.

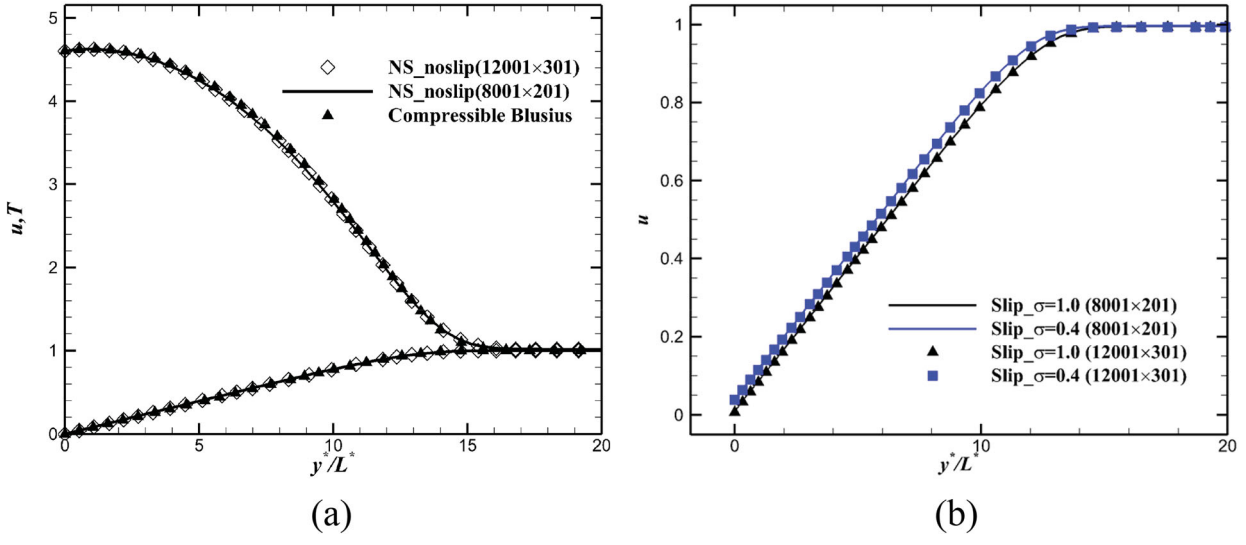

Figure A1. Comparisons of (a) streamwise velocity and temperature profiles calculated by DNS with two mesh resolutions and compressible Blasius solutions at $x^* = 0.746$ m for the no-slip case; (b) streamwise velocity profiles calculated by DNS with two mesh resolutions at $x^* = 0.18$ m for the slip cases.

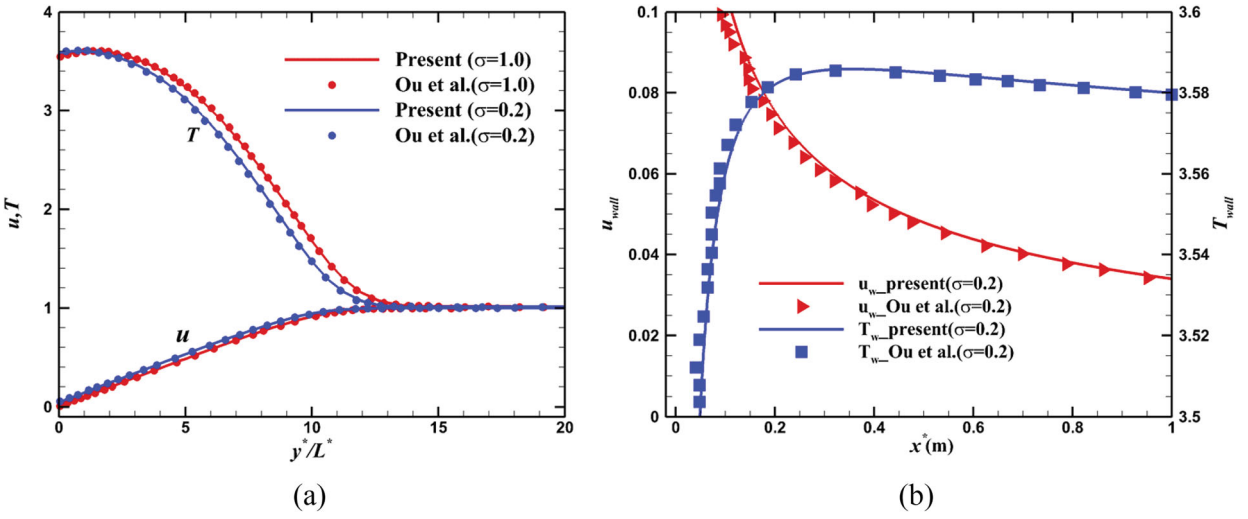

Figure A2. Comparison of streamwise velocity and temperature profiles for slip flow at Mach 4.5 between Ou and Chen (2021) and present results: (a) along the y-axis at $x^* = 0.5$ m; (b) along the plate surface.

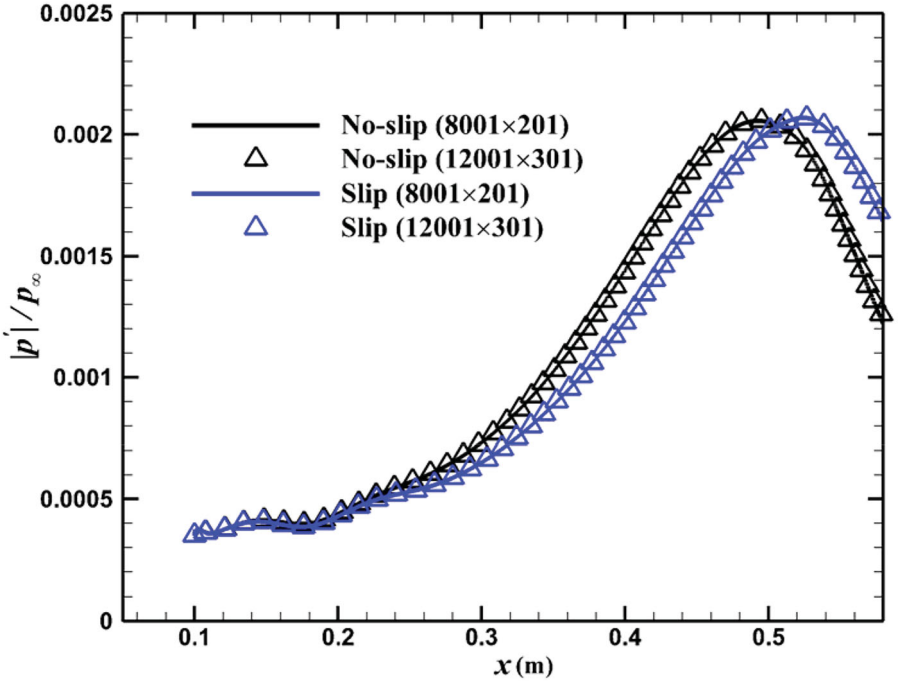

Figure A3. The wall distribution of the amplitude of pressure perturbation for the no-slip and slip ($\sigma = 1.0$) cases with imposed mode S at the inlet of $x^* = 0.1$ m calculated from unsteady simulations using different grid resolution.

Table A1. Comparison of the computed eigenvalues ($\alpha = 0.2$, $\beta = 0$).

Method	Eigenvalue of ω
Klothakis et al.	0.182390-0.003960i
Present	0.181447-0.003928i

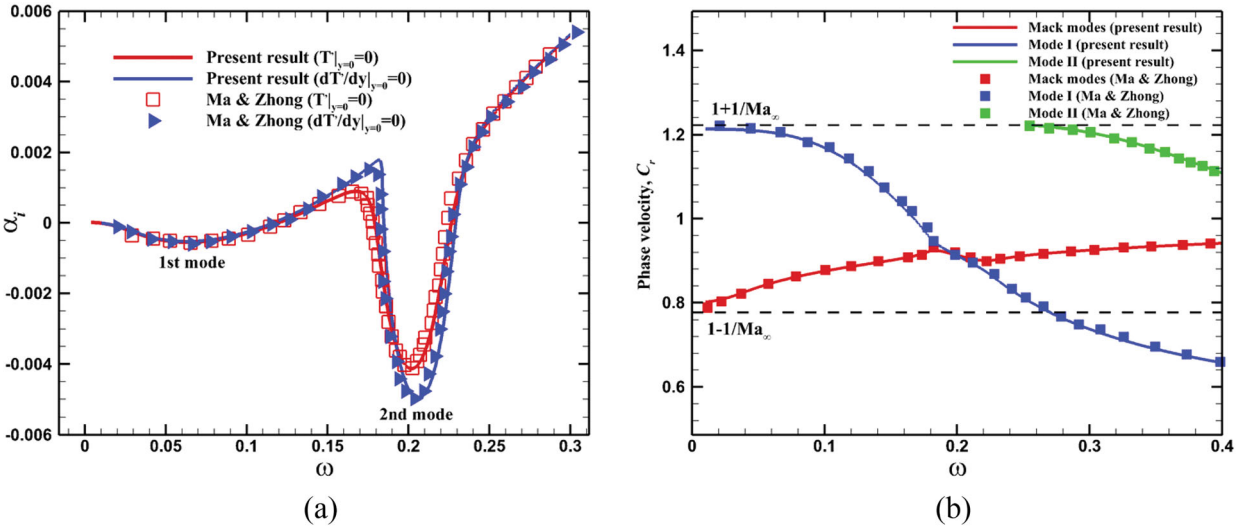

Figure A4. Comparison of growth rates and phase velocities of different modes between the present and Ma and Zhong's (2003a) results. (a) Growth rates with adiabatic and isothermal boundary conditions. (b) Phase velocities with adiabatic boundary conditions.

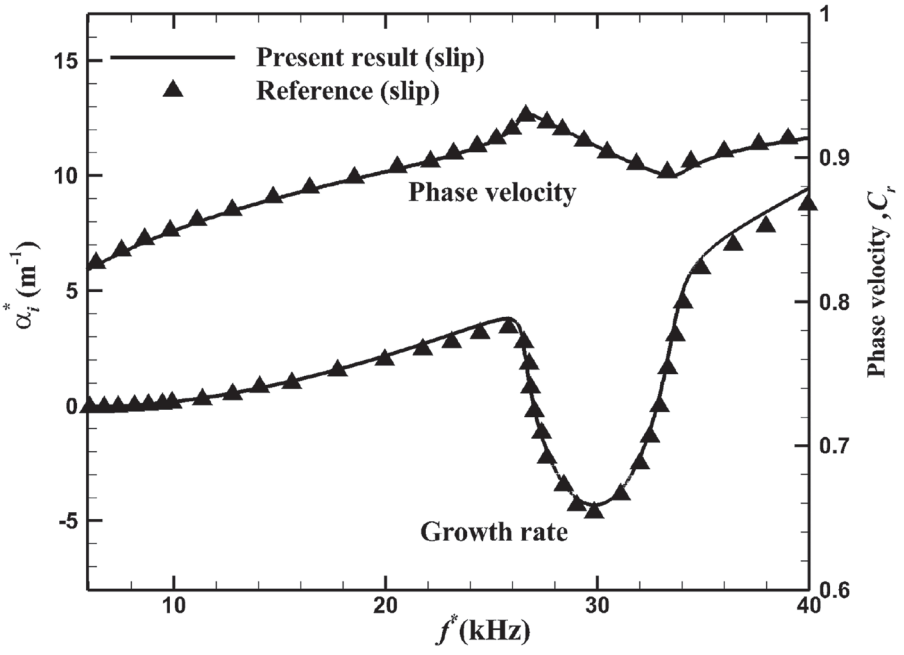

Figure A5. Comparison of growth rate and phase velocity versus frequency at $x^* = 1.0$ m of a two-dimensional wave for the slip flow ($\sigma = 0.2$) obtained by Ref. 5 (BC-1F) and the present calculation.